A521: A cluster forming at the crossing of two filaments?

S. Maurogordato

▶ **To cite this version:**

S. Maurogordato. A521: A cluster forming at the crossing of two filaments?. Astronomy and Astrophysics - A&A, 2000. hal-03026848

HAL Id: hal-03026848
https://hal.science/hal-03026848v1

Submitted on 21 Mar 2022

HAL is a multi-disciplinary open access archive for the deposit and dissemination of scientific research documents, whether they are published or not. The documents may come from teaching and research institutions in France or abroad, or from public or private research centers.

L'archive ouverte pluridisciplinaire **HAL**, est destinée au dépôt et à la diffusion de documents scientifiques de niveau recherche, publiés ou non, émanant des établissements d'enseignement et de recherche français ou étrangers, des laboratoires publics ou privés.

Distributed under a Creative Commons Attribution 4.0 International License

Astron. Astrophys. 355, 461–478 (2000)

ASTRONOMY AND ASTROPHYSICS

A521: A cluster forming at the crossing of two filaments?

M. Arnaud[1], **S. Maurogordato**[2], **E. Slezak**[2], **and J. Rho**[1,3]

[1] CEA/DSM/DAPNIA/Service d'Astrophysique, CEA/Saclay, 91191 Gif sur Yvette Cedex, France (arnaud@hep.saclay.cea.fr)
[2] CERGA, CNRS, Observatoire de la Côte d'Azur, B4229, Le Mont-Gros, 06304 Nice Cedex 4, France (maurogor, slezak@obs-nice.fr)
[3] Present adress: IPAC/California Institute of Technology, Pasadena, CA 91125, USA (rho@ipac.caltech.edu)

Received 25 March 1999 / Accepted 4 January 2000

Abstract. We present ROSAT/HRI and ASCA observations, combined with optical multi-object spectroscopy and photometry of A 521, a rich galaxy cluster at z=0.247.

The ROSAT/HRI image of A 521 shows an irregular morphology with two peaks separated by $\sim 500\mathrm{h}_{50}^{-1}\mathrm{kpc}$. A Wavelet analysis of the X-ray image reveals the presence of two cluster components: a diffuse main cluster, with an emission peak offset from the BCG position and a compact less massive cluster in the North West, probably in an early merger phase with the main cluster. The surface brightness profiles of both components are well fitted by two independent isothermal β-models. The overall cluster temperature derived from the ASCA spectra is 6.4 ± 0.8 keV.

The density of the galaxies in the cluster central part follows an irregular, nearly cross-like, structure. Two main ridges S1 (NE/SW) and S2(NW/SE) cross south of the BCG and belong to the cluster from our velocity measurements. Whence the position of the X-Ray center of the main cluster roughly coincides with the intersection of the optical ridges S1 and S2, the segregation between the gas and the galaxies subclustering is extremely severe. This is an indication of a very particular dynamical state.

Several interesting alignments are apparent. The center of the two X-ray sub-clusters are aligned with the S2 direction as well as the BCG major axis, whereas the main X-Ray cluster is elongated along the ridge axis S1. This last feature, together with the extremely large X-Ray core radius of the main cluster and the very high velocity dispersion within the ridge S1, suggests that a more ancient merger already occurred along direction S1. At larger scale, the ridges S1 and S2 point in the direction of the nearest angular neighbors among Abell clusters: A517 and (A528/A518) respectively.

The observed alignment effects can be most naturally explained if A521 is a young cluster currently forming at the crossing of two filaments, one pointing towards A517 and the other in the direction of A528/A518, along which the cluster is accreting material. The intersection of filaments are thought to be the natural place of rich cluster formation and A521 might be the first observed evidence for this hypothesis.

Send offprint requests to: M. Arnaud

Key words: galaxies: clusters: general – galaxies: clusters: individual: A521 – cosmology: dark matter – X-rays: general

1. Introduction

In hierarchical models of structure formation, the formation of bound objects occur from the collapse of initial density fluctuations that grow under the influence of gravity, and are built from smaller structures that have previously formed. This virialisation process is ongoing now at cluster scale, as indicated by the observed variety of dynamical states of these objects (e.g. Buote & Tsai 1996). Cluster properties therefore still depend on the details of structure formation scenario and their study provides a unique diagnostic on the conditions in the early Universe.

Many analytical and numerical calculations show that the present rate of cluster growth depends strongly on the density parameter Ω of the Universe. This cosmological parameter can thus be constrained in principle from the frequency of substructure in the present day cluster population (e.g. Richstone et al. 1992), provided that subclustering is a reliable indicator of youth or recent accretion and that 'substructure' is suitably quantified. In practice recent attempts to constrain Ω from statistical studies of cluster X-ray spatial morphologies (e.g. Mohr et al. 1995; Buote & Xu 1997) have yield some contradictory results and the reliability of this method is debated (see e.g. Nakamura et al. 1995). It is essential that we understand better the physics of merger events (in particular the intracluster medium relaxation timescale) and their effect on observable cluster properties.

Similarly detailed studies of sub-structures in non relaxed clusters and cluster orientation give us clue to the formation process it-self. In numerical simulations of hierarchical clustering, clusters form preferentially through anisotropic accretion of sub-clusters along large scale filaments (Katz & White 1993; West et al. 1991). The evidence from X-ray data, that subclusters tend to be arranged along a linear structure within clusters, co-aligned with the matter distribution on supercluster scale, gives strong support to that scenario (West et al. 1995). Filamentary structures up to scales of $\sim 100\ \mathrm{h}^{-1}\ \mathrm{Mpc}$ have been unraveled in the cluster distribution (Batuski et al. 1999). Direct evidence of matter infall along a filamentary structure has been given for the first time by Durret et al. (1998)

from their dynamical analysis of the A85/87/89 complex. A related and much debated issue is the general elongation of clusters and their tendency to be aligned with their neighbors. Numerical simulations of van Haarlem & van de Weygaert (1993) suggest that the orientation of a cluster at a given time is fixed more by the direction of the last merger than by the matter distribution at large scale. Thus cluster-cluster alignments would indicate highly anistropic accretion along a main filament, connecting the clusters. On the other hand a cluster accreting matter more istropically at the crossing of several filaments would have an orientation highly variable with time, independently of the orientation of its neighbors.

In this paper we present a study of a highly unrelaxed cluster, A 521. Our analysis revealed very particular morphological and dynamical properties. We discuss possible explanation and its implication for cluster formation.

A 521 is a distant (D=6), relatively rich (R=1), Southern Abell cluster, of Bautz-Morgan Type III (Abell et al. 1989). It is known from the HEAO-1 survey to be a bright X-ray source (Kowalski et al. 1984). It has been observed with the IPC on board the Einstein satellite with a flux of $0.21\,10^{-11}\,\mathrm{erg/s/cm^2}$ in the energy band of 0.7-3.5 keV (Ulmer et al. 1986). It has been suggested (Ulmer et al. 1985) that it could form a binary cluster with its neighbour A518. Radio emission has been found in the area of the cluster (Hanisch & Ulmer 1985). Optical analysis of this cluster has begun very recently with the discovery of a strong gravitational arc candidate in the core of the cluster at CFHT (Maurogordato et al. 1996). We have then undertaken an observational campaign, in order to perform multi-object spectroscopy and multi-band imaging of this cluster. Optical spectroscopic data and a dynamical study based on radial velocities for 41 cluster members is presented by Maurogordato et al. (2000). This study confirmed that A 521 is a moderately distant cluster ($z = 0.247$) and indicates that this cluster is presently undergoing strong dynamical evolution. The two brightest knots of the arc candidate are shown to be at the velocity of the cluster, making the gravitational lensing interpretation for the bright curved structure very improbable. A detailed analysis of the orientation of the galaxies within the cluster is undergoing (Plionis et al. 1999). Here we present ROSAT/HRI and ASCA data and analyze them at the light of the optical spectroscopic data and new photometric data to assess in details the dynamical state of the cluster.

The outline of the paper is as follows: the cluster X–ray morphology and gas distribution is presented in Sect. 2. A wavelet analysis of the HRI image is performed to filter out the noise, unravel significant substructures and separate the various cluster components. The density distribution and mass of the subclusters are derived from a β-model fit to their surface brightness profiles. The ASCA data are used to derive the overall gas temperature. Optical imaging data are presented in Sect. 3. We computed the galaxy iso-density and iso-luminosity map of the cluster, as well as its optical luminosity in the V-band. A detailed comparison of X-ray and optical morphology, as well as a new analysis of the galaxy velocities is made Sect. 4 to compare the galaxy and gas subclustering and study the kinematic and dynamics of the main structures. The dynamical state and formation history of the cluster are discussed in Sect. 5. The main conclusions and implications of our analysis are summarized in Sect. 6. All numbers are expressed as a function of $\mathrm{h_{50}}$, the Hubble constant in units of 50 km/s/Mpc. A deceleration parameter $q_0 = 0.5$ is used in the following. All the errors are at the 68% confidence level for one interesting parameter and computed following the method described by Avni (1976).

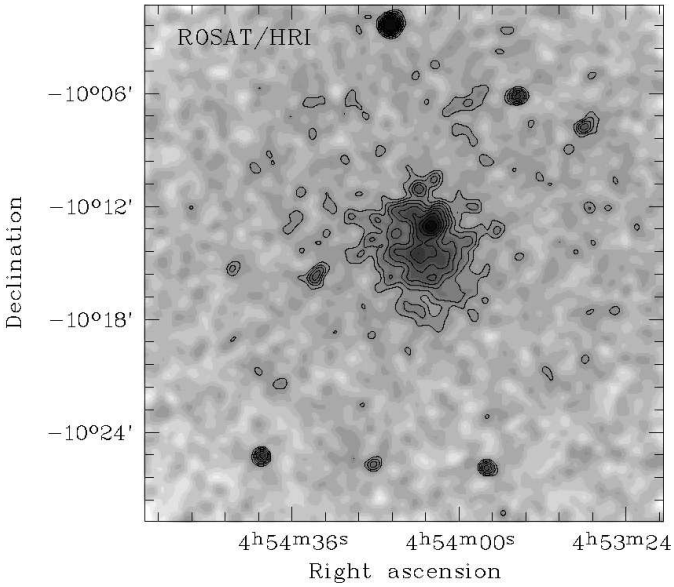

Fig. 1. A deep (45 ks) ROSAT/HRI X-ray image centered on A 521. The pixel size is $5'' \times 5''$. Only photons in channels 2 to 10 are used. The raw image has been smoothed by a gaussian filter of $\sigma = 15''$. The isocontours are logarithmically spaced by 0.05 digits, the lowest contour corresponds to 1.25 ct/pixel.

2. X-ray data analysis

2.1. ROSAT/HRI image

We observed A 521 with the ROSAT High Resolution Imager ($\sim 5''$ angular resolution) for a total of 44.5 ksec between March 10 and 18, 1996.

An image was constructed from the HRI event data, using $10'' \times 10''$ pixels binning and selecting only channels 2 to 10 to minimize particles background. The exposure and particle background maps were constructed using the analysis techniques for extended objects developed by Snowden (1995, 1998).

The HRI image of the $27.5' \times 27.5'$ field centered on the cluster and smoothed with a gaussian filter ($\sigma = 15''$) is shown on Fig. 1. The cluster morphology is irregular. There is a strong peak in the North, offset from the cluster center, and possibly a secondary peak, located south of the main peak. It is thus not obvious from this image if the cluster should be classified as a offset-center cluster or as a bimodal cluster.

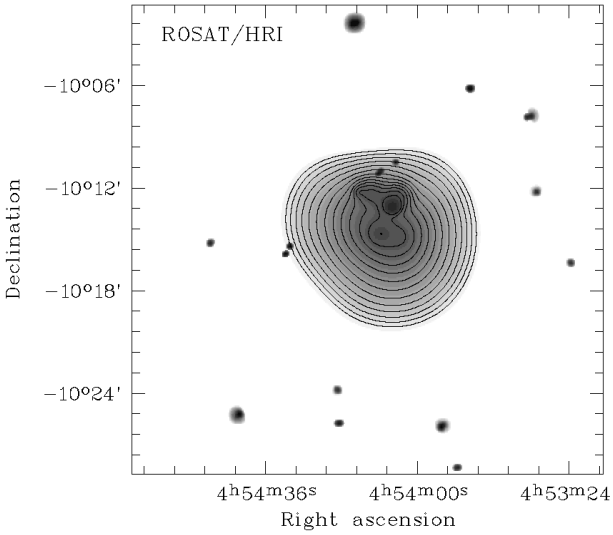

Fig. 2. Restored X-ray image from the wavelet analysis of the HRI raw image. The significance level has been set to 3σ. The isocontours of the cluster are logarithmically spaced by 0.15 digits, the lowest contour corresponds to $2.2\ 10^{-2}$ ct/pixel.

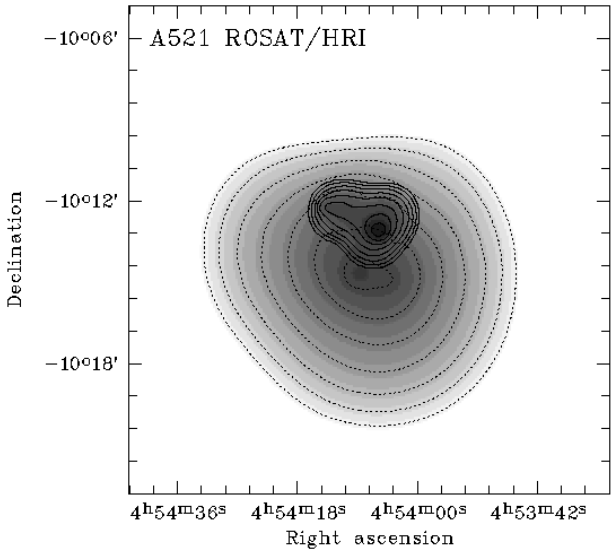

Fig. 3. Restored X-ray image of the cluster from the wavelet analysis of the HRI raw image. The significance level has been set to 3σ. The iso-intensity contours of the reconstructed main cluster (dotted line) and of the compact sub-cluster (full line) are superimposed. The image has been corrected for exposure. The isocontours are logarithmically spaced by 0.3 digits, the lowest contour corresponds to $5.7\ 10^{-5}\mathrm{ct/s/arcmin}^2$.

2.2. Wavelet analysis

Wavelet-based technics have been shown to be very fruitful for the analysis of galaxy clusters, in particular for the X-Ray emission (Slezak et al. 1994; Biviano et al. 1996; Pislar et al. 1997; Lima-Neto et al. 1997; Pierre & Starck 1998; Lemonon et al. 1997; Dantas et al. 1997; Vrtilek et al. 1997) and for the detection of sub-structures in optical galaxy catalogs (Slezak et al. 1990; Escalera et al. 1992; Gambera et al. 1997). Such a multi-scale approach allows one to remove noise by taking into account only significant structures at different spatial scales. A clean image can thus be obtained where structures (objects) of different scales are identified. We have analyzed our HRI image with the Multi-scale Vision Model (MVM) package developed at OCA since several years; a complete description of this method can be found in Bijaoui & Rué (1995), and Rué & Bijaoui (1997). As in Slezak et al. (1994) we explicitly take into account the Poisson statistics and the significance level was set to 3σ.

2.2.1. Point sources

We first detected point sources using an algorithm which involves the amplitude of the wavelet coefficients. Point sources are defined as objects detected at scale 1 or 2 (comparable to the HRI PSF). They are listed in Table 1. We cross correlated their position with the position of the APS objects in the field. Proposed identifications are given in the table. This information will be used below to check the astrometry of the HRI image.

2.2.2. Cluster

The detection of large scale diffuse objects mixed with smaller ones is quite difficult when these latter are much more brighter and compact than the former. For that purpose the wavelet strategy has to be modified by normalizing the coefficients by their energy (Rué & Bijaoui 1997). We used this technique on the image, obtained after subtraction of previously reconstructed point sources. Only one structure was detected, which clearly corresponds to the cluster (see Fig. 2).

To extract possible sub-components, we applied again the multiscale analysis on the ($5' \times 5'$) inner part of the reconstructed cluster. A compact substructure is detected, which is centered on the cluster main peak, at $\alpha(J2000.0) = 4^h54^m5.8^s$, $\delta(J2000.0) = -10°13'04''$. One notes however that its emission is asymmetric, with a tail towards the NE. After subtraction of this component, the cluster appears regular and slightly elliptical in shape. A fit of this image with an ellipsoid gives a PA angle (defined anti-clockwise from North) of $57°$. It is centered at $\alpha(J2000.0) = 4^h54^m8.6^s$, $\delta(J2000.0) = -10°14'39''$

In summary our wavelet transform analysis of the X-ray image revealed the presence of two sub-clusters (see Fig. 3): a diffuse main cluster (hereafter A521S) in the southeast centered on the second X-ray peak (hereafter $\mathrm{X_S}$) and a compact smaller cluster (hereafter A521N) corresponding to the brightest peak (hereafter $\mathrm{X_N}$).

2.3. Intra-cluster medium model

To quantify the gas distribution of the two components, we constructed their azimuthically averaged surface brightness profile, $S(\theta)$, where θ is the angular distance to the center of the component considered. The surface brightness profile was calculated directly from the event file in order to be as accurate as possible

Table 1. Point sources detected in the ROSAT/HRI image and possible identification

ROSAT source				Proposed optical counterpart					
Name	$\alpha(J2000.0)$	$\delta(J2000.0)$	Rate (ct/s)	APS Number APSO_898_	$\alpha(J2000.0)$	$\delta(J2000.0)$	Class	Magn.	D
RXJ0454.2-1002	$04^h54^m14.82^s$	$-10°02'20.4''$	7.27	178355	$04^h54^m14.9^s$	$-10°02'26.5''$	star	18.92	$6.1''$
RXJ0454.7-1025	$04^h54^m42.39^s$	$-10°25'13.2''$	2.49	245025	$04^h54^m42.4^s$	$-10°25'11.9''$	star	17.83	$1.3''$
RXJ0453.9-1026	$04^h53^m54.16^s$	$-10°25'54.0''$	2.06	243729	$04^h53^m54.3^s$	$-10°25'53.0''$	galaxy	19.98	$2.3''$
RXJ0453.8-1006	$04^h53^m47.44^s$	$-10°06'09.5''$	1.86						
RXJ0453.6-1008	$04^h53^m33.28^s$	$-10°07'47.7''$	1.43	206734	$04^h53^m33.7^s$	$-10°07'55.0''$	star	16.63	$9.5''$
RXJ0454.5-1015	$04^h54^m30.18^s$	$-10°15'22.8''$	0.98	207719	$04^h54^m30.2^s$	$-10°15'26.5''$	star	11.44	$3.7''$
RXJ0454.5-1016	$04^h54^m31.19^s$	$-10°15'50.0''$	1.02	207737	$04^h54^m31.3^s$	$-10°15'52.2''$	star	20.83	$2.2''$
RXJ0454.3-1026	$04^h54^m18.52^s$	$-10°25'43.1''$	1.10	244342	$04^h54^m18.6^s$	$-10°25'44.2''$	star	20.20	$1.5''$
RXJ0454.1-1011	$04^h54^m08.91^s$	$-10°11'03.5''$	1.14						
RXJ0453.8-1028	$04^h53^m50.47^s$	$-10°28'19.1''$	0.79						
RXJ0454.8-1015	$04^h54^m49.03^s$	$-10°15'11.4''$	0.67	208038	$04^h54^m49.0^s$	$-10°15'16.8''$	galaxy	20.47	$5.3''$
RXJ0454.1-1010	$04^h54^m05.10^s$	$-10°10'28.5''$	0.62						
RXJ0453.5-1012	$04^h53^m31.71^s$	$-10°12'12.2''$	0.61	206709	$04^h53^m32.2^s$	$-10°12'18.5''$	galaxy	20.34	$6.3''$
RXJ0454.3-1024	$04^h54^m18.87^s$	$-10°23'46.9''$	0.59						
RXJ0453.4-1016	$04^h53^m23.55^s$	$-10°16'20.9''$	0.55						

and to have a cross-check of the above MVM decomposition of the cluster in two components. We selected, as above, only data corresponding to channel 2 to 10 to maximize the signal to noise ratio. We excluded from our sample circular regions centered on the individual point sources and with a radius equal to their angular extent FWHM. The particle background was then subtracted using the background surface brightness profile obtained from the background map. The error on this background level (statistical error) was added quadratically to the statistical error in each radial bin. After particle background subtraction, the profiles are corrected for exposure, using the exposure map.

2.3.1. Main component: A521S

We first considered the main component: we constructed the surface brightness profile centered on $\mathrm{X_S}$, excluding the region of the sub-cluster as defined by our wavelet analysis.

The X–ray diffuse background was then estimated using data in the outer part of the field of view ($5.5' < \theta < 12.5'$). An analysis of the shape of the non-subtracted surface brightness profile showed that the cluster contribution is clearly negligible in that region. The possible systematic error on the background (due to contribution of unresolved point sources ...) was estimated from the fluctuations (1σ value) in the background from ring to ring. The background level was found to be $9.8 \pm 0.8\ 10^{-4}\mathrm{ct/s/arcmin^2}$.

We then binned the data to insure about 1σ significance at least for the count rate in each ring, after X–ray background subtraction. The resulting background subtracted profile is displayed on Fig. 4. The cluster emission is significantly detected up to $1.5\ \mathrm{h_{50}^{-1}\ Mpc}$ at the 68% confidence level. At this radius the cluster brightness is equal to respectively 18% of the background level.

We also constructed the surface brightness profile of the image of the main cluster, as reconstructed by the MVM. It is in excellent agreement with the profile directly derived from the event file (see Fig. 4).

We tried to fit the surface brightness profile,$S(\theta)$, with the so called β model (Jones & Forman 1984):

$$S(\theta) = S_0 \left[1 + \left(\frac{\theta}{\theta_\mathrm{c}}\right)^2\right]^{-3\beta+\frac{1}{2}} \quad (1)$$

where θ is the angular distance to the cluster center and θ_c is the core radius. For an isothermal ICM, this corresponds to a gas density distribution versus radius r given by:

$$n_\mathrm{gas}(r) = n_0 \left[1 + \left(\frac{r}{R_\mathrm{c}}\right)^2\right]^{-3\beta/2} \quad (2)$$

We have taken into account the finite spatial resolution of the HRI by convolving the model with the HRI PSF (David et al. 1993) at the center of the cluster.

The surface brightness profile is well fit by the isothermal β-model (See Fig. 4). The best fit is obtained for $\beta = 0.72$, $R_\mathrm{c} = 630\ \mathrm{h_{50}^{-1}\ kpc}$ with a χ^2 of 3 for 12 degrees of freedom. These parameters are poorly determined (see Table 2), essentially because the emission is only traced out to less than 2.5 core radii. This is consequence of the exceptionally large value of the core radius, which is further discussed in Sect. 5.

2.3.2. Sub-cluster: A521N

We then considered the sub cluster: we constructed the surface brightness profile centered on $\mathrm{X_N}$, using the same procedure as above. However we also have to subtract the contribution of the main cluster. For that purpose a synthetic image of our best

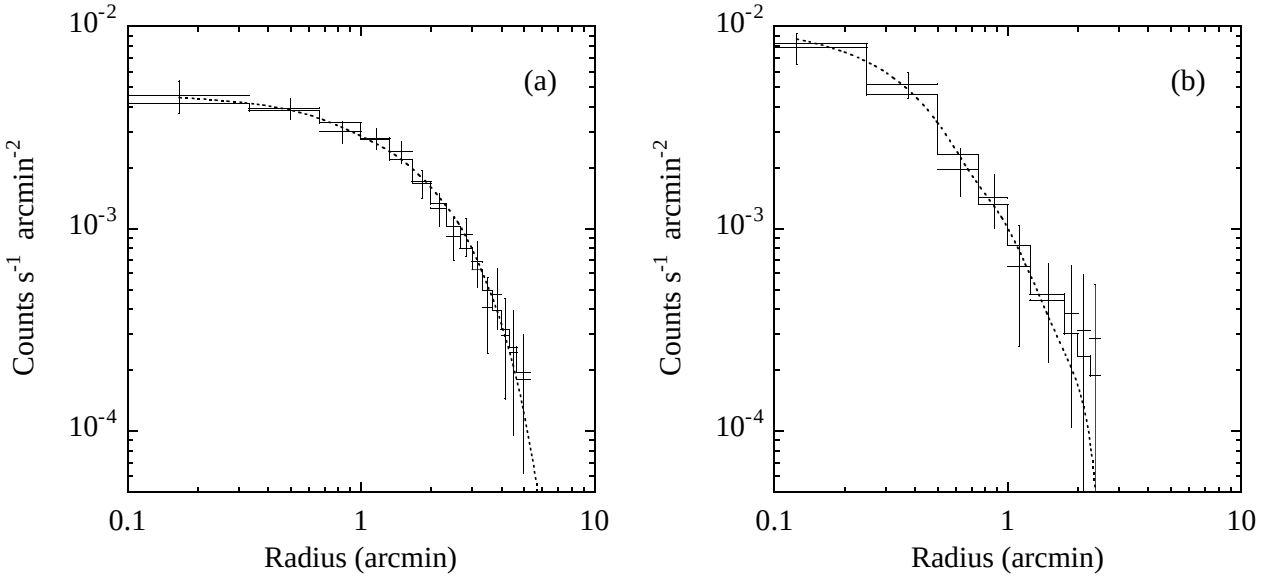

Fig. 4a and b. The X-ray surface brightness profiles of the main cluster (left) and the compact sub cluster (right), corrected for vignetting effect and after background subtraction. The crosses correspond to the data points with error bars derived from the event file. The full line corresponds to the best fit β model: $\beta = 0.71$, $R_{\rm c} = 690\,{\rm h}_{50}^{-1}\,{\rm kpc}$ for the diffuse main cluster and $\beta = 0.52$, $R_{\rm c} = 110\,{\rm h}_{50}^{-1}\,{\rm kpc}$ for the compact subcluster. The dotted line is the profile derived from the wavelet reconstructed images of each component respectively.

fit main cluster β model was generated. Its surface brightness profile, centered on $X_S$was computed and subtracted from the overall profile. We crudely took into account the errors on this model, assuming it is equivalent to the statistical errors in each bin of the model number counts. The subcluster emission is detected up to $2.5'$ ($730\ {\rm h}_{50}^{-1}\ {\rm kpc}$) from its center and within that radius the count rate (0.1-2.4 keV) is $1.5\ 10^{-2}$ cts/s. As can be seen in Fig. 4, the emission of the sub-cluster is much more peaked that the emission of the main cluster. Its central surface brightness is higher than the main cluster one, although its count rate is only $\sim 22\%$ of the main cluster count rate.

We fitted the surface brightness profile of the subcluster with a β model. A good fit to the data is obtained with a χ^2 of 2 for 6 degrees of freedom. The derived β and core radius are: $\beta = 0.5$ and $R_{\rm c} = 95\,{\rm h}_{50}^{-1}\,{\rm kpc}$, typical of the values found for groups.

We also constructed the surface brightness profile of the image of this subcluster, as reconstructed by the MVM. It is again in excellent agreement with the profile directly derived from the event file (see Fig. 4).

The good agreement between the profiles derived from the event file and from the MVM reconstruction, together with the fact that the profiles of both components are well fitted by classical β models, further support the presence of two X-ray clusters: a large diffuse cluster A521S and a compact smaller cluster A521N. We cannot tell however at that stage if these two components are dynamically bound or are chance superposition of physically independent clusters.

2.4. Temperature measurement using ASCA data

ASCA observation of A521 took place Feb. 11-13, 1996 for $\sim$100 ks. The useful exposure time, after classical filtering based on the orbital paremeters, (elevation, earth occultation, geomagnetic Cut off rigidity (COR)) and instrumental parameters, is 42 ks and 40 ks for the data taken with the two Gas Imaging Spectrometers (GIS) and the two Solid-state Imaging Spectrometers (SIS) respectively. The cut-off rigidity is an estimate of the momentum per elementary unit charge which a particle must have to penetrate from infinity to a given point in the Earth magnetosphere. The background induced by charged particle varies with the satellite position, and is anti-correlated with the Cut off Rigidity value. We have generated background files using blank sky observations, weighted according to the Cut Off Rigidity (in GeV/c) values; COR=10–12 for 40% of the A521 data, COR=12–14 for 31% and COR=8–10 for 13%. This weighting improves the accuracy of the background estimate, which is important for a proper temperature determination. The total count rates of GIS2 and SIS0 are 0.08 ± 0.0015 and 0.189 ± 0.002 cts s^{-1}, respectively.

The GIS image in Fig. 5 shows that the cluster morphology is irregular. There is some indication of two peaks in the center, in agreement with the HRI image. However the peaks are poorly resolved with ASCA. Furthermore their positions appear about $40''$ offset from the HRI position, while the uncertainty in the astrometry for this observation is about $1.3'$ due to errors in the tracking reading. In view of the complex morphology of A521 revealed by the HRI observation and the ASCA astrometry uncertainties, we did not attempt to estimate the temperature of the two sub-clusters separately. The determination of the relevant extraction region and the necessary correction for the finite PSF would be highly uncertain. We concentrate in this paper on the overall cluster spectrum. We considered a circular extraction region, of $5'$ in radius, centered on $\alpha(J2000.0) = 4^h54^m4.3^s$, $\delta(J2000.0) = -10°14'10''$.

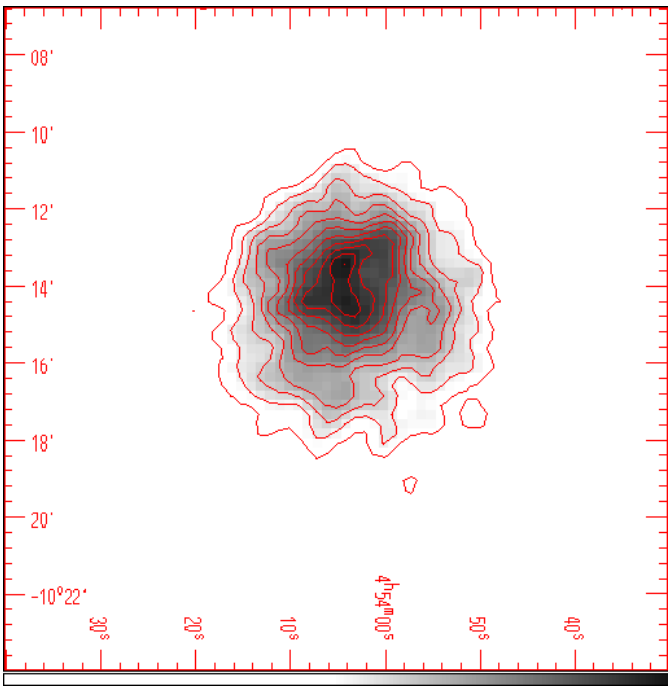

Fig. 5. The smoothed ASCA GIS image of A521; the GIS2 and GIS3 images are combined. The contours are $0.275 - 1.25\,\mathrm{counts/s/arcmin^2}$ and the difference between adjacent contours is 0.0975. The image is smoothed by a gaussian filter with $\sigma = 15''$.

Table 2. Physical parameters of the main and sub cluster as derived from ROSAT/HRI data

Parameter		Main	Subcluster
HRI Count rate	(ct/s)	$6.8\ 10^{-2}$	$1.5\ 10^{-2}$
$S_{\rm X}$	$(\mathrm{ergs/s/cm^2})^{\rm a}$	$3.6\ 10^{-12}$	$8.1\ 10^{-13}$
$L_{\rm X}$	$(\mathrm{h_{50}^{-2}\ ergs/s})$	$9.4\ 10^{44}$	$2.1\ 10^{44}$
$n_{\rm H}^0$	$(\mathrm{h_{50}^{1/2}\ cm^{-3}})$	$1.6\ 10^{-3}$	$5.7\ 10^{-3}$
β		$0.72^{+0.30}_{-0.15}$	$0.50^{+0.14}_{-0.07}$
$R_{\rm c}$	(arcmin)	$2.2^{+0.9}_{-0.6}$	$0.32^{+0.18}_{-0.12}$
	$(\mathrm{h_{50}^{-1}\ kpc})$	630^{+260}_{-170}	95^{+50}_{-35}
$R_{\rm max}$	(arcmin)	5.3	2.5
	$(\mathrm{h_{50}^{-1}\ Mpc})$	1.5	0.73
$M_{\rm gas}(\leq R_{\rm max})$	$(\mathrm{h_{50}^{-5/2}\ M_\odot})$	$1.8\ 10^{14}$	$2.6\ 10^{13}$

[a]: in the [0.1–2.4 keV] energy band

The GIS and SIS spectra are shown in Fig. 6. We fitted these spectra simultaneously with a thermal redshifted emission model. The normalization between the two spectra was let free and the redshift was fixed at the optical value of $z = 0.247$. We obtained a best fit reduced χ^2 of 1.1, a hydrogen column density $N_{\rm H} = 8.2 \pm 4.\ 10^{20}\ \mathrm{cm^{-2}}$, a temperature $\mathrm{k}T = 6.3 \pm 0.8\ \mathrm{keV}$, and a heavy element abundance of 0.14 ± 0.12 relative to cosmic values. The given errors are at the 90% confidence level. We also fitted the GIS and SIS spectra independently. The derived fit parameters from each detector well agree to each other. The $N_{\rm H}$ value is not well constrained and is consistent with the value derived from the 21 cm measurement, $N_{\rm H} = 5.4\ 10^{20}\ \mathrm{cm^{-2}}$ (Dickey & Lockman 1990). If we adopt this value, a slightly higher best fit temperature is obtained, $\mathrm{k}T = 6.9\ \mathrm{keV}$, which is well within the 90% confidence interval for this parameter.

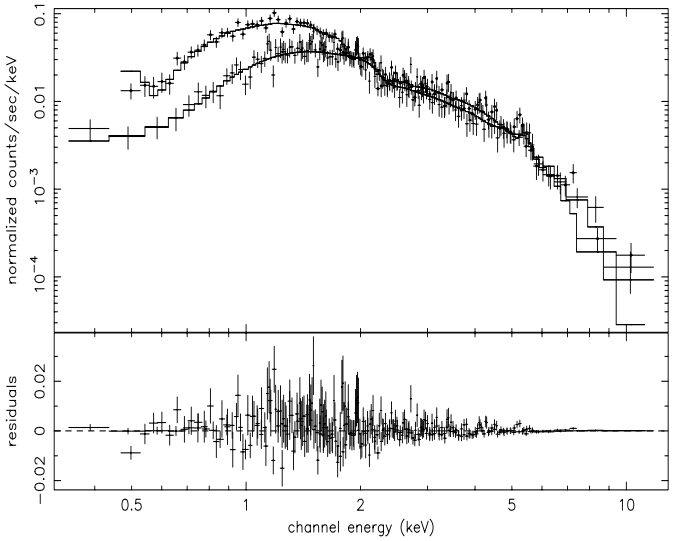

Fig. 6. The spectra of GIS and SIS of A521: the best spectral fit with one-temperature thermal model is superposed, and the residual are also shown.

2.5. Luminosity and gas mass

From the known HRI response and the observed count rates we deduced the flux and luminosity of the two cluster components, using a thermal redshifted emission model. We used the ASCA determined temperature and the hydrogen column density deduced from 21 cm measurements. From the profile shape parameters values obtained above from imaging data, we can then deduce the central hydrogen density of each sub-cluster and their gas mass. The results are summarized in Table 2. With a total luminosity of more than $10^{45}\ \mathrm{h_{50}^{-2}\ ergs/s}$, A521 is a luminous cluster. We also note that the mass of the sub-cluster is typical of the mass of a group and amount to a significant fraction (about 15%) of the main cluster mass.

The total flux in the [0.1-2.4] keV energy band determined with ROSAT translates into a flux of $0.38\ 10^{-11}\ \mathrm{ergs/s/cm^2}$ in the Einstein [0.7-3.5] keV energy band, using the emission model described above. This is nearly twice the value obtained from the IPC data by Ulmer et al. (1986). However the IPC pointing was significantly offset, the cluster was positioned very close to the IPC rib, in the heavily vignetted part of the field of view. This could explain part of the discrepancy. The same computation in the ASCA [0.4-10] keV band gives an expected ASCA flux (corrected for absorption) of $0.71\ 10^{-11}\ \mathrm{ergs/s/cm^2}$, 40% higher than the measured value of $0.5\ 10^{-11}\ \mathrm{ergs/s/cm^2}$. Although the ASCA extraction region is large, we could have missed some cluster flux due to the large ASCA/PSF. Moreover several temperature components are probably present. In particular if the sub-cluster is cooler than the main cluster, the conversion factor between the HRI and the ASCA band may be overestimated by our simple computation. However we cannot

exclude that the systematically higher value of the flux obtained with the ROSAT/HRI may be due in part to systematic errors in the HRI data. A maximum error on the HRI flux of 40% would imply only an error of $\sim 20\%$ on the gas mass and thus the impact on the determination of this parameter is small. Moreover the HRI instrument is the most reliable to derive gas masses: count rates are nearly independent on temperature and can be readily translated into emission measure; no flux correction is needed for the regions considered due to its excellent spatial resolution. We thus keep the values given in Table 2 derived from HRI data.

3. Optical imaging

3.1. Observations and data reduction

The optical data come from the analysis of a 2048×2048 CCD exposure of 15 mn taken in the V band at CFHT with MOS instrument in March 1997. The main characteristics of the STIS2 CCD are: a pixel size of $\sim 0.44''$ (21μm); gain factor and read-out noise values equal to 4.52 electrons/adu and 8 electrons respectively. The seeing conditions were quite excellent, with a measured half-width at half-maximum for stars around 1 pixel. The frame has been corrected for distortion, bias subtracted and flat-fielded using a mean flat built from 10 exposures. It appears that the borders of the bias-corrected and flat-fielded V image suffers from vignetting. Incomplete detection with wrong shape and flux estimates will result inside this area. To remove most of this under-illuminated zone, the image has therefore been trimmed to a central 1312×1312 square corresponding to a $\simeq 9.6' \times 9.6'$ field of view. At last, a set of three bad columns has been tentatively corrected by a linear interpolation across the columns, both on the flat and on the astronomical exposures. Photometric calibration has been done with standards measured from the NGC 4147 field (Friel et al. 1987).

3.1.1. Object detection

Most galaxies has been found in the trimmed image using classical algorithms for the detection and classification. Let us summarize hereafter the main steps of this approach (see Slezak et al. 1998 for details).

First, an optimal smoothing has been performed in order i) to decrease the background fluctuations which otherwise may lead to spurious detections and ii) to improve the identification of stars through more accurate shape and flux measurements of ascribed gaussian-like objects.

Second, since each single object is defined as a set of adjacent pixels with intensity above the sky background higher than a preset value, a background map was computed by interpolating mean values coming from intensity histograms inside boxes large enough to be background dominated. This way, large-scale background variations such as the low-intensity east-west gradient we found in the flat exposure are taken into account, and a homogeneous detection is insured across the whole field. Erroneous high background mean estimates occurring for boxes where most pixels belong to very bright (hence large) objects were replaced by the median of the undisturbed neighboring estimates, so that detection of some faint galaxies around bright stars was made possible. However, in most cases, the detection of what can be named embedded objects is beyond reach of such a mono-scale vision. A multithresholding technique may help for deblending components (Bertin & Arnouts 1996), but a total solution requires a real multiscale approach. So, to get a complete catalogue, such a solution based on wavelets (Rué & Bijaoui 1997) has been chosen when necessary.

Third, once detected, we measured each object using i) the low-order moments of its (intensity-weighted) pixel distribution to get basic shape information (center, ellipticity, position angle) and ii) an intensity profile computed from the pixel values inside elliptical annuli with increasing semi-major axis to obtain: an accurate estimate of the local sky background, more sophisticated shape indicators (equivalent radii, gradients, concentration indices, distances to a theoretical stellar profile), and more flux information (peak, central and average brightness, aperture and isophotal magnitudes, asymptotic total magnitude).

3.1.2. Object classification

Finally, objects have to be classified with respect to a synthetic classifier according to expected values or established behavior for each kind of sources, either interactively or in a fully automated way. Before, one must i) select criteria on their ability to discriminate among morphological classes, especially at faint flux levels, ii) remove correlation between indicators to increase the decision robustness, and iii) take into account the statistical errors on the measurements to properly handle each object. Besides, since morphological classes merge unavoidably as the differences between the objects soften with decreasing size and flux, a choice between competing completeness and purity of the final catalogues has to be made according to subsequent studies. Based on these various considerations, the petrossian total magnitude (see Sandage & Perelmuter 1990) and a shape indicator involving the central brightness together with an isophotal radius and the related isophotal magnitude (see Le Fèvre et al. 1986) appeared to bring most of the relevant information for identifying galaxies among stars and image defects (e.g. cosmic rays). So, we decided to classify objects in this two-dimensional parameter space mostly. The test is straightforward since the shape parameter can be normalized to unity for a gaussian-like object whatever its total magnitude is.

3.1.3. Multi-scale approach

Close objects are merged into one single large object when the detection threshold used in the classical approach is lower than the intensity of the saddle point linking the two sets of pixels. Besides, this detection threshold considers background values interpolated from a background map computed with a given scale and not the true local background value related to each object whatever its scale is; it results that the detection peak intensity limit may slightly vary from place to place. Both problems can be overcome by means of a wavelet-based image processing,

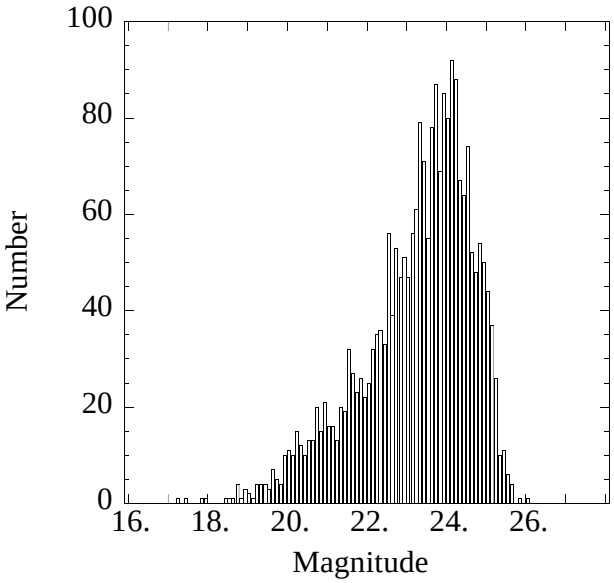

Fig. 7. Magnitude distribution in the V band of the galaxy candidates in our CCD field. Note that the objects fainter than V=24 have not been classified.

as described within the Poisson statistics case in Slezak et al. (1994). According to this multiscale approach, an object with a given size is detected at the spatial scale where its wavelet coefficients are the greatest taking into account values expected from the noise at each scale. This allows one to bypass the background map computation in the detection process and to detect every members in a set of overlapping objects. In order to recover the information missed or merged by the classical detection technique, we therefore applied this method to get another catalogue of astronomical sources. By cross-checking this catalogue and the former one, genuine new objects were identified as well as previously embedded ones. Only their coordinates were recovered this way. For both kind of objects, the shape information required to compute the azimutally-averaged intensity profile needed for photometry and classification has been obtained by fitting an ellipsis on the object radii along twelve directions. These radii result from a dedicated algorithm processing the luminosity profiles for these peculiar angles. Then, the classification procedure described for the isolated objects has been used in a straightforward way since the same photometric and morphological information as before was available.

3.1.4. The catalog

In order to get a catalogue including most of the objects within the image (galaxies as well as stars), the object detection has been performed using the usual segmentation technique with a 1.5σ threshold above the sky background. Almost 2,500 objects were identified using this classical approach, out of which about 110 appeared to be merged objects. The multiscale strategy we applied after disentangled these overlaps into 268 single sources, while also exhibiting 212 new faint sources. The efficiency of the morphological classifiers we used appear to break down around $V \sim 24$, about one magnitude and a half above the faintest objects detected ($V \simeq 25.5$). Taking into account uncertainties in the flux and shape information, we therefore classify only objects brighter than $V = 24$ into several morphological classes: nebular object, stellar object, faint object, cosmic and false detections. The stellar population was found to be 114 objects, while 520 objects fainter than $V = 24$ remained unclassified. Merging the nebular and faint classes in order to be conservative, we were able to define a catalogue of 1,521 galaxies, including 5 nuclei features within the halo of the central bright galaxy of the A 521 galaxy cluster. A final check against the APS database has been performed. It allowed us to remove 8 APS stars which appear elongated on our CCD frame and were therefore correctly misclassified as nebular objects from our package. Hence, our catalogue of galaxies for A 521 includes 1513 objects brighter than $V = 24$. The differential luminosity distribution of the list of non star-like objects indicates that this sample of galaxies is quite complete down to the classification limit, ie. the $V = 24$ magnitude (see Fig. 7).

3.2. Astrometry

The astrometry of the CFHT image has been performed thanks to the GASP package under STDAS. We have retrieved from the APS a catalog of 112 objects with equatorial coordinates guaranteed with a precision better than $0.5''$ within the CFHT field. From this catalog, we have selected a sub-sample of 41 stars or starlike objects, preferentially non saturated and with a circular symmetry, that we have then identified on our CFHT image. We have then run a plate solution program, and obtained the values of the conversion matrix which indicates a small rotation of 1.8 degree. We have therefore rotated the CFHT image and reiterated the previous sequence. The final r.m.s. on the coordinates is of $\sim 1''$. We have checked that this value does not vary systematically within the field.

3.3. The galaxy distribution in optical

The galaxy distribution within and around A 521 has been first examined by means of number galaxy maps built from our photometric catalogue complete down to $V \simeq 24$. We made use of the algorithm first described by Dressler (1980) where the local density value at each location is obtained from the distance encompassing a fixed number of nearest galaxies. Hence, the same statistical weight is given to each density value, but density enhancements with different spatial scales are more or less exhibited according to the chosen number $N_{\rm gal}$ of neighbors. For our galaxy catalogue, it appeared that $N_{\rm gal} = 10$ was well suited to map structures at intermediary scales; the corresponding density maps for several magnitude limits ($V = 22, 23$ and 24) are displayed in Fig. 8. Edge effects were taken into account by means of the area actually available for the computation of the Dressler density.

As a general result at all magnitudes, the overdensity region known as A 521 looks highly anisotropic. We do not detect any smooth or regular structure up to the largest scales available

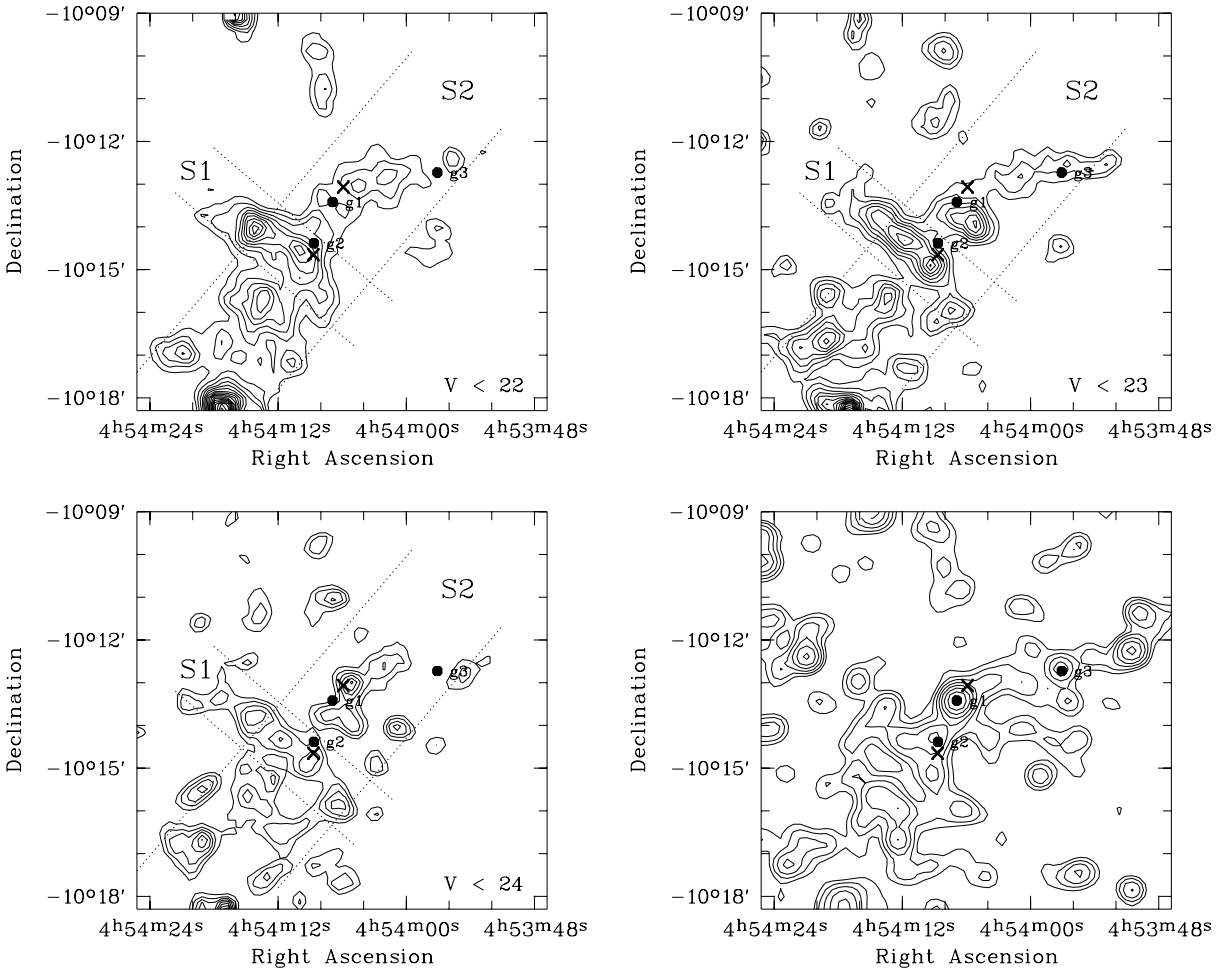

Fig. 8. Galaxy iso-density contours for different cut in magnitudes: $V < 22$ (top left), $V < 23$, (top-right), $V < 24$ (bottom-left). The lowest contour corresponds to 1σ level above the mean density in the field, the contours are spaced by 0.5σ. The iso-luminosity contours are also shown (bottom-right). The iso contours are logarithmically spaced by 0.15 digits. These maps are derived from an analysis (see text) of the $9.6' \times 9.6'$ optical image in V-band obtained at CFHT in March 1997. The main giant elliptical galaxies of the cluster are identified as g1(BCG), g2, and g3, and the positions of the X–Ray maxima $X_N$and $X_S$are displayed as crosses.

from our field of view. The top-left panel of Fig. 8, involving all galaxies brighter than $V = 22$, can be directly compared to the adaptative kernel map obtained in Maurogordato et al. (2000). The various clumps identified by the 3-group KMM partition are clearly present. The central structure identified as the KMM2 partition appears here, thanks to the higher resolution of the maps, to be composed of various clumps.

Going deeper in magnitudes ($V = 23$, Fig. 8 top–right) allows to better define the general pattern of the cluster. South of the BCG and extending from North-East to South-West, there exists a well-defined ridge of galaxies (S1), while a set of over-densities merging together (S2) spreads linearly from North-West to South-East. The former is roughly centered on the Abell coordinates of the cluster, while the latter seems to extend up to the edges of our CCD frame ($\sim$ 3 Mpc at the redshift of the cluster). These two perpendicular features intersect in a cross-like shape south of the BCG at roughly the Abell center for the cluster. S1 shows clearly at least two main clumps at the various magnitude cutoffs investigated. The structure S2 exhibits in its North-West part a large high-density structure made of galaxies with $22 < V < 23$, with the BCG at its North-East border. The region around the BCG is of course more clustered when the nuclei features within its halo are introduced in the computation. Several clumps of galaxies can also be evidenced across most of the field. Their relationship with the main structural components is still pending due to the lack of available redshifts inside these regions.

The main characteristics of this peculiar distribution remain much more the same when galaxies fainter than $V = 23$ are included (bottom-left panel of Fig. 8) with only an increased contrast between low- and high-density regions. However, one must notice that a well-defined new clump of these faint galaxies appears North-West of the BCG in structure S2, centered on $\alpha(J2000.0) = 4^h54^m5.1^s$, $\delta(J2000.0) = -10°13'00''$, very close to X_N.

We have calculated the optical barycenter from our photometric catalog in the V-band. It is located at $\alpha(J2000.0) = 4^h54^m8^s$, $\delta(J2000.0) = -10°13'56''$ for the $V < 23$ galaxies.

The barycenter computed with other magnitude limits differ by less than $5''$. The barycenter does not coincide with the location of the BCG, as it could have been expected, but lies between this galaxy and the second brightest galaxy g2. It is slightly above the crossing of the linear structures S1 and S2.

Finally, the major axis of the three brightest elliptical galaxies g1 (BCG), g2, g3, are found to be aligned with the orientation of the filamentary structure S2, following its progressive bending in the West part of the frame.

The distribution of the galaxies has also been investigated using luminosity density maps computed from their V magnitude. To do so, we decided to simply add the individual luminosities inside identical square areas. Obviously, high-density peaks in local V luminosity were located on the brightest elliptical galaxies within the field. We have dropped out the bright galaxy at coordinates (73.577,-10.236), which was identified as a foreground object by spectrometry (Maurogordato et al. 2000), as its strong luminosity strongly contaminated the isoluminosity map and led to a misleading clump in the Eastern region. Besides, it appeared that the luminosity distribution delineates roughly the same structural features as those seen in the number density maps (bottom–right panel of Fig. 8).

3.4. Total luminosity

We have then calculated the total luminosity of the cluster in the maximum area covered by the CCD field with reliable estimate of the magnitudes. For this purpose, we have to take into account several delicate problems as the subtraction of the background, the correction for limiting magnitude and the K-correction.

As our field is too small to reach sufficent large scales to measure the background from our data, we have estimated the projected number of field galaxies by 0.5 magnitude bin from the deep counts, $N_f(V)$ of the ESO-Sculptor Redshift Survey (Arnouts et al. 1997). In order to correct for the field contamination, we have used a large number of 'background corrected' catalogs for the cluster, created from our original galaxy catalog by rejecting randomly $N_f(V)$ objects in each bin of magnitude, and estimated the luminosity for each realization, by summing the individual luminosity of the remaining objects up to the limiting magnitude of our sample ($V_{\rm lim} = 24$). The magnitude of the remaining objects have been K-corrected and absorption-corrected following Maurogordato et al. (2000), assuming they belong to the cluster. This procedure has been reiterated $N_{trial} = 1000$ times, and the final luminosity is estimated as the mean of the luminosities for the N_{trial} realizations, with a 3σ rejection. This procedure should statistically eliminate the contribution to the total luminosity from the field galaxies.

We have then multiplied the result by the following ratio in order to take into account the faint end of the luminosity function:

$$S = \frac{\int_{M_{V_{\rm lim}}}^{\infty} L\phi(L)dL}{\int_{-\infty}^{\infty} L\phi(L)dL} \qquad (3)$$

For this purpose, we have used the luminosity function in the V-band measured in the ESO-Sculptor Survey (Galaz 1997) with the following parameters for the Schechter function: $\alpha = -1.14$, $M_v^* = -20.61 + 5log(\mathrm{h_{50}})$, $\Phi^* = 0.0229\ \mathrm{h_{50}^3\ Mpc^{-3}}$. At our limiting magnitude of $V_{\rm lim} = 24$, corresponding to $M_v^* + 3.2$, we should reach 92% of the total luminosity of the cluster. This gives a total interpolated V luminosity inside $1.3\ \mathrm{h_{50}^{-1}Mpc}$ centered on $\mathrm{X_S}$ of $L_{\rm V}(< 1.3\ \mathrm{h_{50}^{-1}\ Mpc}) = 1.17\ 10^{13} \pm 1.09\ 10^{11} \mathrm{h_{50}^{-2}\ L_\odot}$. This corresponds, assuming a typical mean mass over luminosity ratio of $< M/L > = 5$, to a total stellar mass within a sphere of radius $1.3\ \mathrm{h_{50}^{-1}Mpc}$ of $M_{\rm star} = 4.22\ 10^{13}\ \mathrm{h_{50}^{-1}\ M_\odot}$. We have here converted the mass estimate in a cylinder derived from the luminosity estimate into a mass estimate within a sphere, using a King model for the galaxy distribution with a core radius derived from the X-Ray analysis (Table 2.). Using the method described in Sect. 2 to calculate the gas mass in the same region we obtained $M_{\rm gas} = 1.45(\mathrm{h_{50}^{-5/2}\ M_\odot})$. This leads to $M_{\rm gas}/M_{\rm star} \sim 3.4\ \mathrm{h_{50}^{-3/2}}$ in the central area of radius $1.3\ \mathrm{h_{50}^{-1}\ Mpc}$. This value is typical of rich clusters (Arnaud et al. 1992).

4. Combined X–ray and optical analysis

4.1. Optical - X–ray relative astrometry precision

To check the astrometric precision of the X–ray image of A 521, confirmed optical counterparts of the X–ray point sources are needed. In the field of view of the CFHT image we found only one such source, RXJ0454.1-1011 (Table 1) which coincides with two interacting galaxies (labelled gA in Fig. 10). The X–ray source has two maxima and is clearly elongated in the direction of the interaction axis of the galaxies thus the identification is secure. The offset between the X–ray position and the optical position of gA, determined from our astrometry of the CFHT image, is $\sim 2''$. With only one source we cannot check independently rotation and translation errors. Outside the CFHT image the most secure identification is RXJ0454.5-1015 with $\mathrm{APS0\_898\_207719}$, which is a very bright star. The offset between the X–ray position and APS position is $3.7''$.

In conclusion we can safely consider that the X–ray astrometry is accurate to better than $\sim 4''$. The precision of the superposition of the HRI image to the CFHT image is probably slightly better.

4.2. Optical and X–ray subclustering

Fig. 9 permits a direct confrontation of the optical and X–ray isocontours maps. The first evidence is that the gas and galaxy distributions are very dissimilar. The galaxy distribution (many clumps organized along 2 nearly perpendicular ridges) is much more irregular than the gas distribution (an essentially regular cluster with a compact sub-cluster) and there is no obvious coincidence between X–ray and optical substructures. We will now examine these points in details.

The BCG is located on the line defined by the X–ray peaks $\mathrm{X_N}$–$\mathrm{X_S}$, $26''$ South-East of $\mathrm{X_N}$, and $1.3'$ North-West of $\mathrm{X_N}$. These values are too large as compared to the precision of our astrometry (see Sect. 4.1) to be allowed to attribute the observed

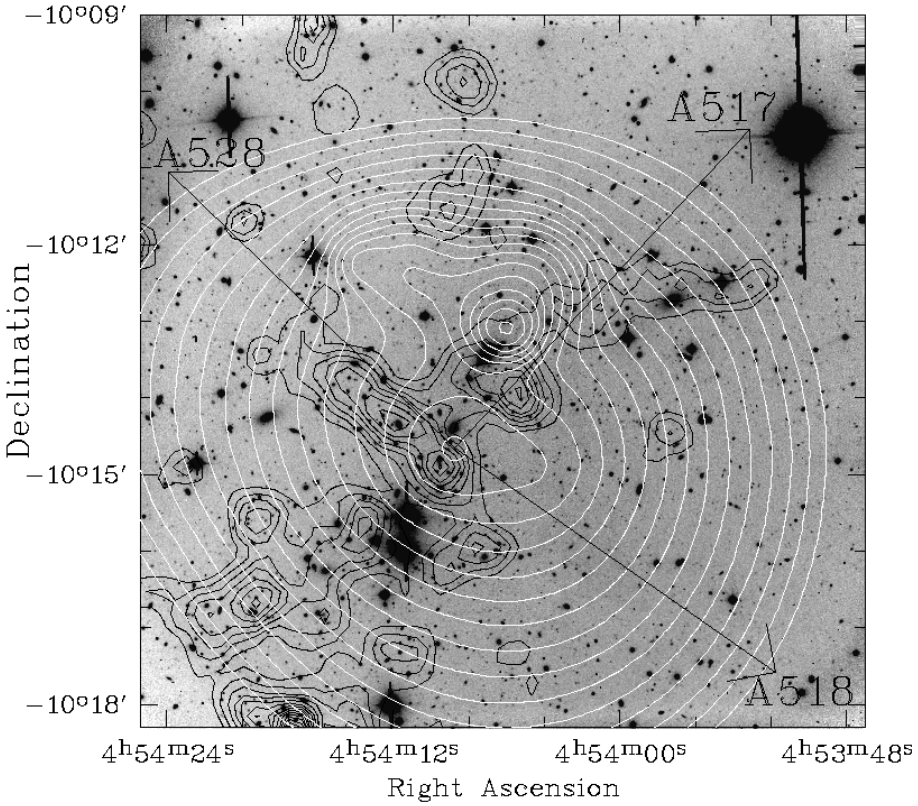

Fig. 9. Galaxy iso-density contours ($V < 23$ black line) and X–ray iso-intensity (white line) are superimposed to the optical image in V-band obtained at CFHT. Contour levels are as in Fig. 2 and Fig. 8 respectively. The direction towards the clusters A517, A528 and A518 are also indicated.

offset of the BCG from any of the X–ray maxima to astrometrical uncertainties. These angular values correspond, at the redshift of the cluster to respectively $158\ \mathrm{h}_{50}^{-1}$ and $475\ \mathrm{h}_{50}^{-1}$ kpc. On the other hand the center, $\mathrm{X_S}$, of the main diffuse X–ray component, A521S, is located roughly at the intersection of the optical ridges S1 and S2. In other words the optical and X–ray overall centroids seem to be coincident. $\mathrm{X_S}$ is also very close to the second brightest galaxy g2, at a distance of only $89\ \mathrm{h}_{50}^{-1}$ kpc South. However the X–ray distribution is very flat in that region (see Fig. 4) and it is difficult to say if this offset is real or not.

There is no optical counterpart in our galaxy iso-density map of the main diffuse and nearly circular symmetric X–ray component which spread all over the CFHT image. However it must be emphasized that the existence of such a diffuse galaxy distribution at large scale is difficult to assess with our present optical data. This is due to the limited field of view of our optical image and the poorer contrast of optical imaging as compared to X–ray imaging, which scales as the density squared. We note however that the main X–ray structure A521S is aligned with S1.

Fig. 10 displays a zoom on the CFHT V-band image centered on the compact X–ray substructure, A521N, with ROSAT/HRI iso-intensity contours superimposed. As discussed in Sect. 2.3 the X–ray emission morphology is typical of a poor cluster. The maximum of the X–ray emission, $\mathrm{X_N}$ is nearly centered on two faint galaxies $30''$ North of the BCG and shows a tail towards North-East with no particular optical counterpart. Galaxy iso-density maps at brighter magnitudes than $V = 23$ do not show any strong maximum in this area (Fig. 9), except for the system around the BCG when the various knots are taken into account. However, when taking into account fainter galaxies at $23 < V < 24$, one notices a strong ($> 4\sigma$) maximum nearly centered on $\mathrm{X_N}$ (Fig. 10) corresponding to the clump mentioned in Sect. 3.3.

Finally we note that, except possibly for the above clump, the various optical clumps apparent in the ridges S1 and S2 have no specific X-ray counterparts. In particular there is no X–ray counterpart of the North-West extension of S2 around the bright elliptical galaxy g3. Similarly the well-defined clumps in the South-East region of S2 corresponding to KMM2 south and KMM3 have no X–ray counterparts.

4.3. Alignment effects

Whereas the optical and X-ray substructures are not coincident, they are not distributed at random. Several strong alignments effects are quite striking and define two privileged axes. The first axis corresponds to S1, coaligned with the orientation of the main X–Ray cluster. The second one corresponds to the alignment between S2, the direction $\mathrm{X_N}$–$\mathrm{X_S}$, the axis of the BCG galaxy, and the axis of the g2 galaxy at the intersection of S1 and S2.

Subclustering orientation has been shown to be frequently correlated with supercluster environment (West et al. 1995). In view of the privileged directions evidenced by both the distribution of galaxies and gas within this cluster, we have investigated the distribution of Abell clusters around A 521. Six Abell clus-

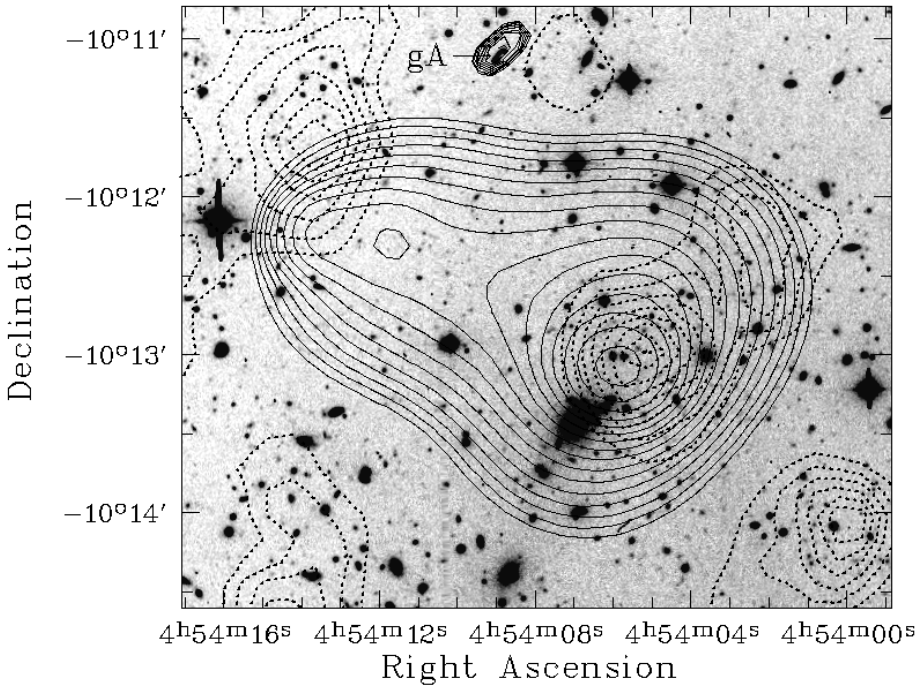

Fig. 10. The region of the X–Ray compact sub-cluster: A521N. Iso-contours calculated on the ROSAT/HRI image are superimposed on the CFHT V-image. The isocontours are logarithmically spaced by 0.1 digits, the lowest contour corresponds to $2.8\ 10^{-4}\mathrm{ct/s/arcmin^2}$. The iso-density contours of galaxies with $23 < V < 24$ are plotted in dashed lines. The lowest contour corresponds to 1σ level above the mean density in the field, the contours are spaced by 0.5σ.

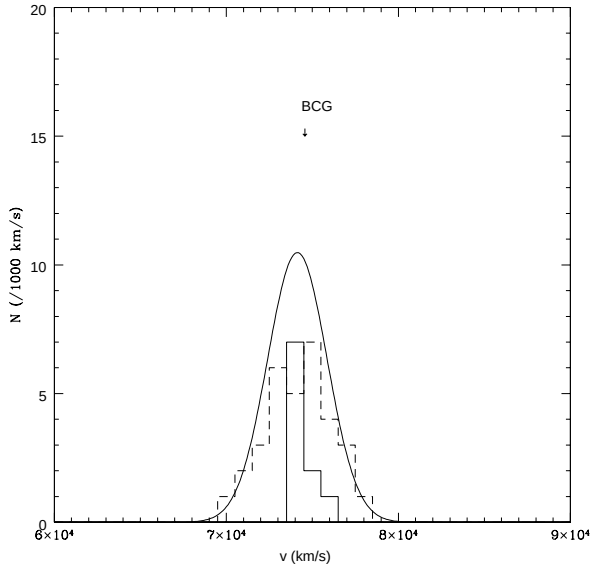

Fig. 11. The radial velocity histogram (binning 1000 km/s) for the two regions centered respectively on X_N (full line) and X_S (dashed line). The region centered on X_S is $30''$ in radius and includes the BCG galaxy plus the three components,A1, C, and D, identified by Maurogordato et al. (2000) and associated with it. The continuous line corresponding to the Gaussian fit for the whole distribution (Maurogordato et al. 2000) is superimposed.

ters of richness $R \geq 0$ are found within a circle of 2 degrees centered on A 521, of which four with $R \geq 1$. In Table 3 are listed the properties of these clusters. The columns are as follows: Columns (1) (2) (3) and (4): identification name, Right ascension and Declination (J2000.0) and richness of the cluster in the ACO catalog (Abell et al. 1989); Columns (5) (6) and (7): redshift estimate, number of redshifts measured by cluster, and reference; Column (7) gives the angular distance of each cluster to A 521 in arcmin and Column (9) the corresponding distance in h_{50}^{-1} Mpc, assuming all the clusters are at as the same redshift z ~ 0.25. Column (10) gives the distance to A521 calculated using the measured redshift given in Column (5).

The directions towards these clusters are indicated on Fig. 9: the striking result is that the direction of S1 is aligned with the axis A521/A517, and S2 with the axes A521/A518 and A521/A528. Comparing then the value of the local to the mean projected density of Abell clusters on the sky, overdensities of $\Delta\sigma/\sigma$ of 4.2 and 7.5 are reached respectively for the $R \geq 0$ and $R \geq 1$ clusters. This suggests that A 521 might be located in a region of high density such as a supercluster. This has however to be verified in redshift space. The values of the distances to A 521 based on the present redshift measurements listed in Column (10) are quite large. In particular A516 and A513 are very probably foreground clusters. However, the redshifts quoted for most cluster corresponds to very few galaxies (1 to 4 in the best case), and can then be considered to be uncertain. Distances to A 521 assuming that the clusters are at the same redshift lies within $\sim 20 - 40\ \mathrm{h_{50}^{-1}\ Mpc}$. These values are typical of superclusters (Batuski & Burns 1985; Batuski et al. 1995). In order to clear up if a real overdensity do exist, the measurement of at last ten galaxy redshifts by cluster allowing a definitive estimate of the mean redshift of each cluster is required.

4.4. The velocity dispersion and the X-ray temperature

The measured velocity dispersion (1386^{+206}_{-136} km/s, Maurogordato et al. 2000) can be compared to the value expected from the mean σ–T_X relation. Under the hypothesis that the gas and the galaxies are in dynamical equilibrium within the cluster potential, the ratio between their specific energies is expected to

Table 3. Main optical properties of ACO clusters in the periphery of A 521

Abell Number	$\alpha(J2000.0)$	$\delta(J2000.0)$	**R**	**z**	N_z	**Ref**	θ (arcmin)	D_1 (h_{50}^{-1}Mpc)	D_2 (h_{50}^{-1}Mpc)
A 521	$04^h54^m10.1^s$	$-10°15'11''$	1	0.2470	41	4	0.0	0	0
A 518	$04^h51^m21.6^s$	$-10°42'59''$	2	0.1804	4	1	49.9	18.0	300
A 517	$04^h50^m29.3^s$	$-09°13'56''$	2	0.2244	1	1	81.9	29.8	102.8
A 513	$04^h48^m10.8^s$	$-09°42'46''$	0	0.1491	1	1	94.2	34.4	448.8
A 516	$04^h50^m05.8^s$	$-08°48'54''$	1	0.1411	2	3	105.2	—-	490.2
A 528	$04^h59^m17.5^s$	$-09°00'32''$	0	0.2896	1	2	106.4	38.8	183.6

References: 1. Struble & Rood (1987); 2. Strubble & Rood (1991); 3. Quintana & Ramirez (1995); 4. Maurogordato et al. (2000)

be constant and equal to: $\beta_{\rm spec} = \sigma^2/({\rm k}T/\mu{\rm m_P})$, where μ is the mean molecular weight and $\rm m_P$ is the proton mass.

Using the value of X-ray temperature determined from ASCA, $kT = 6.3 \pm 0.8$ keV, we are led to $\beta_{\rm spec} = 1.9^{+0.8}_{-0.5}$. This value is high as compared to the mean value $\beta_{spec} = 0.94 \pm 0.08$ obtained by Lubin & Bahcall (1993) from a sample of 41 clusters with more than 20 redshifts of galaxies measured by cluster. The expected value of the velocity dispersion using our measurement of kT and assuming $\beta_{\rm spec} = 1$ would be $\sigma = 1017 \pm 65$ km/s. The high velocity dispersion as compared to the ICM temperature suggests that A 521 is far from equilibrium, as discussed in more details in Sect. 5.2

4.5. Dynamics of the galaxies within the high-density regions

In the previous section, several high density regions have been evidenced both in X-Ray and in optical. Using the measured velocities of galaxies we now study their kinematic and internal dynamics. The redshift analysis of the three substructures in the optical distribution identified by the kernel map and the KMM analysis can be found in Maurogordato et al. (2000).

An important question is whether the two X–ray components, A521N and A521S are dynamically bound or are chance superposition of independent clusters. We have thus split the redshift data into two sets associated to each region and studied their redshift distribution.

For A521N, we have considered all the galaxies with measured redshifts within a given area around its X-ray center $\rm X_N$. We have first focused on the inner part, within $30''$ of the center. This region includes 6 galaxies within the cluster, among them the BCG galaxy and the two small galaxies nearby $\rm X_N$. All these galaxies have magnitudes brighter than $V = 22$ so this do not involve the galaxies contributing to the strong peak evidenced at $V > 23$. Applying the ROSTAT package (Beers et al. 1990), we derived values of $v_{BI} = 74363^{+170}_{-260}$ km/s and $\sigma_{BI} = 500^{+160}_{-60}$ km/s. These values are very tentative as the number of redshifts is very small. We have then re-calculated these quantities adding the three components A1, C, and D, close to the BCG, identified by Maurogordato et al. (2000) and which were shown to have secure redshifts within the cluster. The results remains stable: $v_{BI} = 74303^{+63}_{-425}$ km/s and $\sigma_{BI} = 416^{+120}_{-92}$ We have also taken into account a larger area (up to $\sim 1'$) to gain a few objects. This however increases the risk of including members candidate of the main cluster. We obtained $v_{BI} = 73974^{+314}_{-218}$ km/s and $\sigma_{BI} = 765^{+250}_{-140}$. This is consistent with the values obtained for the KMM1 partition, which corresponds to a region of similar size, slightly offset North-West: $v_{BI} = 74124^{+289}_{-232}$ km/s and $\sigma_{BI} = 806^{+682}_{-240}$ km/s (Maurogordato et al. 2000). As expected from the small number of objects considered, the values of the velocity dispersion are fluctuating significantly and more velocities are necessary to converge to the real estimate.

For A521S, we considered the whole set of cluster members centered on $\rm X_S$, excluding the first set associated to $\rm X_N$. This results in a sample of 32 galaxies, with a location of $v_{BI} = 74170^{+240}_{-345}$ km/s and a very high velocity dispersion of $\sigma_{BI} = 1550^{+220}_{-170}$ km/s.

Our data indicate that, within the errors, there is no significant velocity offset between the galaxies in the A521N and A521S regions.

The mean velocity is also consistent with the BCG, which is at the mean velocity of the whole system (Maurogordato et al. 2000). On the other hand the velocity dispersion around $\rm X_N$ seems to be significantly smaller than around $\rm X_S$. These results are clearly illustrated by the histogram of velocities displayed in Fig. 11. The precision of our analysis is of course limited by the small number of velocities measured in the $\rm X_N$ region.

We then considered the two density ridges S1 and S2 and isolated the galaxies with measured redshifts in these structures. For S1, the selected galaxies are those used in the KMM2 North partition. Values obtained by Maurogordato et al. (2000) are $v_{BI} = 74122^{+552}_{-650}$ km/s and $\sigma_{BI} = 1995^{+330}_{-230}$. For S2 we avoided the central region, which crosses S1, and were left with 18 galaxies. We obtained $v_{BI} = 73867^{+175}_{-292}$ km/s and $\sigma_{BI} = 900^{+360}_{-110}$, which is consistent with the values for KMM1 and KMM2 South, which are included in S2. It appears that S1 and S2 have the same mean velocity within the errors. S1 presents a huge velocity dispersion, about twice the value obtained for S2.

5. Discussion

5.1. Which structures do belong to the A521 cluster?

The measured mean velocity of the high density ridges S1 and S2 are not significantly different (Sect. 4.5). They are thus both substructures of the A521 galaxy cluster. However we have not

enough velocity measurements to say if some of the individual clumps along the ridges are chance superpositions.

Although its morphology is very different from the galaxy distribution, we can reasonably consider that the X-ray main structure A521S corresponds to the ICM associated with A521 galaxies. The fact that its maximum is located at the crossing of the 2 optical ridges (Sect. 4.2) is consistent with this idea, as well as the corresponding overall gas mass over luminosity ratio, typical of a rich cluster (Sect. 3.4).

The X-ray compact substructure A521N could correspond to a foreground or background cluster or to a sub-cluster dynamically linked to A521. We have thus investigated which optical counterpart could be physically associated to it.

The simplest hypothesis one can do is that A521N is associated with the structure of faint galaxies at $23 < V < 24$, which is nearly centered on the X-ray peak $\mathrm{X_N}$ (Sect. 4.2 and Fig. 10). Unfortunately we do not have redshift measurement for any of these galaxies. Let us first assume that this structure belongs to the cluster. We have then calculated the luminosity of galaxies fainter than $V = 23$ in an area of radius 1 arcmin centered on $\mathrm{X_N}$. The radius size has been chosen in order to cover the maximum possible extent of A521N without crossing the optical ridge S1. The value of the luminosity obtained $L_\mathrm{V} = 6.18\ 10^{10}\ \mathrm{h_{50}^{-2}\ L_\odot}$ ($L_\mathrm{V} = 7.03\ 10^{10}\ \mathrm{h_{50}^{-2}\ L_\odot}$ without background correction) is very low. This corresponds to a stellar mass estimate $M_\mathrm{star} = 2.35\ 10^{11}\ M_\odot$. However, at these faint magnitudes the background subtraction is essential. Background correction has been performed as in Sect. 3.4 using the deep V-counts by Arnouts et al. (1996). This assumes that the cluster is located in a region which is representative of the field. If it belongs to a local over-density as for instance a supercluster, the background will be under-estimated, and the luminosity over-estimated (the opposite situation would occur if it is located in a low-density region). The following measurements of the luminosities are then tentative as long as we do not have estimates of the local background at the periphery of the cluster. We can thus infer that the estimate of the stellar mass as compared to the gas mass estimate is too low to attribute the X-Ray emission A521N only to the optical overdensity at $23 < V < 24$: the gas mass calculated in the same radius $M_\mathrm{gas} = 5.5\ 10^{12}\ \mathrm{h_{50}^{-5/2}\ M_\odot}$ would lead to an unreasonably high ratio $M_\mathrm{gas}/M_\mathrm{star} \sim 23\ \mathrm{h_{50}^{-3/2}}$. We have shown in Sect. 4.3 that there are some pieces of evidence that A521 belongs to a supercluster. This would increase the previous $M_\mathrm{gas}/M_\mathrm{star}$ discrepancy.

The second hypothesis we have investigated is that A521N is still linked to the $23 < V < 24$ structure but that this excess of faint galaxies is produced by a background cluster. In this case the visible mass corresponding to the integrated luminosity of the previous galaxies would be greatly enhanced as a result of the highest redshift, but this effect would in principle be strongest for the gas mass. However, as the redshift increases, one expects that the galaxies with $23 < V < 24$ sample the luminosity function of the cluster more at the brightest end. As a matter of fact, the factor one has to multiply the integrated luminosity of galaxies brighter than $V = 24$ in order to recover the total luminosity of the cluster (which is very near to unity at $z = 0.25$) becomes very important at high redshift. It is therefore not possible from our present data, to exclude the possibility of a background high redshift ($z > 0.5$) cluster on the basis of the comparison of the stellar and of the gas mass. Deep, multi-band exposures associated to more sophisticated counts taking into account the evolutionary effects are necessary to test this last hypothesis.

The last possibility is that A521N is associated to the whole set of galaxies around the BCG galaxy including the previous western overdensity of faint galaxies. In that case A521N would be a component of A521, the bright galaxies of that region being at the mean cluster redshift (Sect. 4.5). This hypothesis naturally explained the fact that $\mathrm{X_N}$ is located on S2, a region of galaxy overdensity, whereas if A521N is a background cluster such a coincidence is unlikely. The inferred luminosity is $L_\mathrm{V} = 1.2\ 10^{12}\ \mathrm{h_{50}^{-2}\ L_\odot}$. This value lead to a reasonable ratio $M_{gas}/M_\mathrm{star} \sim 1.3\ \mathrm{h_{50}^{-3/2}}$ which is within the range expected for a poor cluster of galaxies (Arnaud et al. 1992). The velocity dispersion in that region (which is considered as a preliminary result in view of the small number of galaxies involved) is significantly smaller as compared to the main cluster (Sect. 4.5) and is too typical of a poor cluster. The only may be surprising fact in that scenario is that the Brightest Galaxy is associated with the sub-cluster instead of the main cluster. In conclusion we think that the most likely picture in view of the present data set is that A521N is indeed a subcluster of A521.

5.2. A521 a dynamically young cluster

There are clear indications that A521 is dynamically young. The first obvious evidence is the the irregular morphology of the gas and galaxy distribution. The second is the high velocity dispersion and β_{spec} value. If the cluster is far from equilibrium, both σ and T can be biased indicators of the potential. For instance, the gas may be not fully thermalized as shown in simulations in the case of merging processes, thermal gradients are expected, and the presence of velocity subclustering can strongly overestimate the velocity dispersion. The large value, $\sim 600\mathrm{h_{50}^{-1}kpc}$, obtained for the core radius of the main cluster is another indication that the system is far from being relaxed (Jones & Forman 1999), as well as the presence of numerous radio sources (see Appendix).

In the following section we propose a tentative scenario to explain the very peculiar morphology of A 521, in particular the strong segregation between the X-ray gas and the galaxies, together with the alignment observed. The X-ray bimodal morphology, with two well defined cluster-like components, suggests a classical picture where a group, A521N, is falling onto a main cluster, A521S. On the other hand the galaxy distribution suggests that we are seeing a cluster currently forming at the crossing of 2 filaments, along which the cluster is accreting material. This would naturally explain the irregular cross-like structure (many clumps organized along two nearly perpendic-

ular ridges) and the alignment observed with the direction of nearby clusters. The dynamical analysis of Maurogordato et al. (2000) also favor this scenario. An obvious question is whether these scenario for the gas and the galaxies are consistent.

5.3. A tentative formation scenario

The large core radius of the main X-ray cluster A521S is typical of clusters, like A2256 (Briel & Henry 1994) or A2255 (Burns et al. 1995), which are thought to have recently undergone a merger event. It is natural to assume that if a recent merger has indeed occurred in A521S, the collision axis is one of the direction privileged in the optical map, i.e. along S1 or S2.

Although the recent history of the ICM in A521S is certainly more complex that the merger of two isolated initially relaxed sub-clusters, we can tentatively compare our observation with numerical simulations of such events (Schindler & Muller 1993; Roettiger et al. 1997). As indicated by these simulations, the behavior of the collisional gaseous component is very different from the behavior of the collisionless dark matter (or galaxies) components (see Fig. 23 in Roettiger et al. 1997). While the galaxy distribution is always elongated along the merger axis (see also Haarlem & de Weygaert 1993), the elongation of the gas varies with time. It is elongated perpendicular to the merger axis soon after core passage and generally parallel later on. After core passage, the X-ray centroid lies between the centroids of the two DM components, while they remain distinct before settling into a relaxed common configuration.

The first hypothesis we examined is that A521S is the result of the recent merger, along S2, of two subclusters centered on the two brightest galaxies g1 (BCG) and g2. This is consistent with the elongation of A521S perpendicular to S2. However this is in contradiction with the hypothesis, supported in Sect. 5.1, that the BCG is associated with A521N. Furthermore the position of the X-ray center, $\mathrm{X_S}$, is not located between g1 and g2, as would have been expected in this scenario.

Alternatively we can be witnessing the later stage of a merger which occurred along S1, in agreement with the elongation of A521S parallel to this axis. We further note that $\mathrm{X_S}$ lies in between the two main clumps apparent in the S1 ridge, which could correspond to the galaxy merging sub-units. Additional support to this last scenario is given by the very large velocity dispersion in the S1 ridge, as discussed in Maurogordato et al. (2000). After the collision epoch the velocity dispersion along the merger axis reaches its maximum value, which can be twice the equilibrium value (Schindler & Böhringer 1993). The velocity data can be explained if the collision axis, projected on the sky in the direction S1, presents a significant (e.g. $\sim 45\,\mathrm{deg}$) angle with the plane of sky.

The subcluster A521N still appears as a clearly distinct unit in X–ray and the corresponding velocity dispersion is small. A521N is probably in a pre-merger phase with A521S. The alignment between the direction defined by the two X–ray peaks, $\mathrm{X_N}$–$\mathrm{X_S}$, the orientation of the BCG (assumed to be associated with A521N) and the filamentary structure S2 is naturally explained if the collision occurs along S2. Furthermore the merging must occur nearly in the plane of the sky, otherwise one should expect to detect a signature of the merging velocity on the radial velocities. In this scenario, we can further speculate on the offset between the X-ray peak, $\mathrm{X_N}$, and the BCG. The BCG is likely to follow the DM dynamics during infall. On the other hand, the gaseous component is submitted to ram pressure by the ICM of the main cluster and might lag behind the DM component. This would qualitatively explain the relative position of $\mathrm{X_N}$, $\mathrm{X_S}$ and the BCG along the S2 axis. However, one would also expect a bunching of the iso-photes along S2 in the S-E, due to ram pressure. Only a slight compression perpendicular to S2 in the S-W is observed instead. Similarly this scenario fails to explain the N-E tail of X-ray emission in the A521N image, which is nearly perpendicular to the assumed collision axis. Such tail, which has been observed for instance in the core of Coma, could arise during the interaction of the merging group with the main cluster, as the gas is ram pressure stripped or the dark matter is tidally disrupted (Vikhlinin et al. 1997). One would thus expect that such tail lies paralell to the collision axis, behind the falling group. Thus although the A521N isophotes seem distorded as expected if A521N is an infalling group, their orientation remain puzzling. We must emphasize however that the exact morphology of A521N is still uncertain: the number of detected counts is still small (~ 700) and the derived morphology might depend on the exact reconstruction of the main cluster.

In summary, there is evidence that A521 is accreting both gaseous and galaxy material along the S1 and S2 structures. A reasonable assumption is that the X-ray subcluster A521N is falling along S2, while the main cluster has formed recently by mergers along S1. Both the X-ray and optical data do favor a scenario where A521 is forming at the crossing of two filaments.

Even in the framework of our interpretation, one could be surprised that the galaxy distribution still follows a filamentary structure in the very central part of the cluster. The fact that the galaxy distribution is much more clumpy than the gas distribution is also puzzling. First we must be cautious in view of the limitations in our data. As already mentioned, the two ridges may well be embedded in a diffuse galaxy component at large scale, which could not be detected with our present optical data. Similarly faint sub-structures in the X-ray map might have been missed by the HRI, due to its limited sensitivity. Second linear structures are not uncommon in observed galaxy clusters. The S2 structure, which comprises the three brightest galaxies, arranged approximately collinearly with clumps around them, is reminiscent of the morphological type L (line) in the classification of Strubble & Rood (1982). About 20% of nearby clusters falls in this category. Finally the interaction between collisional components is more violent and disruptive than between collisionless components (see e.g. Roettiger et al. 1997). This might qualitatively explain the longer survival of optical substructures and their alignment along a filamentary structure if the accretion occurs along a privileged direction (i.e. along a filament present at larger scale).

6. Conclusions

We have presented new X-ray and optical data on the distant cluster A521. This cluster has unique properties, indicative of a very particular dynamical state. In X-ray it appears as a classical bimodal cluster, but the brightest peak is associated with the less luminous component. The optical morphology is very peculiar, with two elongated high density clumpy ridges defining a cross like structure. The BCG, although at rest within the potential of the cluster, is not centered on any of the two X-Ray maxima. It is also significantly offset from the optical barycenter. The segregation between the gas and galaxy subclustering is extremely severe. On the other hand strong alignment effects, from galaxy to supercluster scale, are observed. They define two privileged axes, along the two optical ridges, pointing in the direction of the nearest angular neighbor clusters.

From a combined morphological and dynamical analysis we argue that the structures observed are not simply due to chance superposition of physically independent units. Our interpretation of the present data is that A521 is a very young cluster currently forming at the intersection of two filaments, along which the cluster is accreting both gaseous and galactic material. The intersection of filaments are thought to be the natural place of rich cluster formation (e.g Katz & White 1993) and A521 might be the first observed evidence for this hypothesis. Its study can thus give us crucial information for our understanding of cluster formation.

Further observations, both in X-ray and optical, are required to confirm our interpretation and fully understand the physics of this exceptional cluster. Planned AXAF observation will allow us to study the gas thermal structure, which is a strong indicator of the evolutionary state. In particular the collision of two subclusters should manifest itself by characteristic features in the temperature maps. We will also be able to resolve more accurately the morphology of the gas distribution, and thus understand better the segregation between the different cluster components.

Acknowledgements. We are very grateful to Albert Bijaoui, Benoit Vandamme and Frédéric Rué for their help in the analysis with the more recent version of MVM. We benefitted from very fruitful discussions with J.P. Chieze, G. Evrard and S. Schindler on cluster formation and evolution, which helped us to clarify our understanding of this cluster. We thank all the A521 collaborators, T.Beers, A.Cappi, J.Kriessler, D. Proust and R. Pello for having given us the opportunity of making this analysis before the publication of the velocity data.

This research has made use of the APS Catalog of POSS I, the NASA/IPAC Extragalactic database (NED), the Digitized Sky Survey and the NRAO VLA Sky Survey (NVSS, Condon et al. 1998). The APS Catalog of POSS I is supported by the National Science Foundation, the National Aeronautics and Space Administration, and the University of Minnesota. The APS databases can be accessed at http://aps.umn.edu/. NED is operated by the Jet Propulsion Laboratory, California Institute of Technology, under contract with the National Aeronautics and Space Administration. The Digitized Sky Surveys were produced at the Space Telescope Science Institute under U.S. Government grant NAG W-2166. The images of the DSS are based on photographic data obtained using the Oschin Schmidt Telescope on Palomar Mountain and the UK Schmidt Telescope.

Part of this work was supported by CNES, INSU and CEA through the "Programme National de Cosmologie".

Appendix A: Comparison to radio 20 cm map

The analysis of the radio-emission properties of the cluster brings a complementary information which can be used to study the dynamical connection between the hot gas and the relativistic electrons. A comparison of radio and X-Ray properties of a sample of 41 clusters has been done by Burns et al. (1994), who showed the existence of an angular correlation between X-Ray sub-clumps and radio galaxies, and between the presence of a WAT associated to the BCG and an elongation of the central X-Ray emission.

Several cases of galaxy clusters showing evidence of merging processes at the optical and X-Ray wavelengths, have been shown to reveal very interesting radio features as for instance the presence of distorted or tailed objects (A 2555, Feretti et al. 1997; A 2634, Pinkney et al. 1993). The orientation of these objects can be used to shed some light on the distribution of the orbits of galaxies inside the cluster. In very rare cases (Coma, Perseus, A 2255 ...), a cluster-wide radio halo has been detected, whose interpretation is still under debate, but in which merger processes have been recently suggest to play a key role (Feretti & Giovannini 1996).

As mentioned by Hanisch & Ulmer (1985), the region of A 521 is rich in radio sources. We have searched the NVSS Source Catalog produced by the 1.4 GHz NRAO VLA Sky Survey (Condon et al. 1996). This survey has detected 19 radio-sources brighter than 2.5 mJy in a 30' field centered on the position of the BCG. This corresponds roughly to the inner Abell radius of the cluster. Table A.1 lists in Column 1 the identification number of the source for this paper, in Columns 2 and 3 right ascension and declination in J2000.0 as listed from NVSS, and in Column 3 the integrated flux density in a Gaussian centered on each source provided by the NVSS, as well as the deconvolved values of the Major and minor axes in Columns 4 and 5. Column 6 gives the NVSS identification of the source. We have extracted via the WEB from the NVSS (Condon et al. 1998) the Stokes I corrected image of this field. The radio image has a $\theta = 45''$ FWHM resolution, and is sampled with a 5" pixel spacing. Fig. A.1 shows a superposition of the corresponding radio isocontours with a 30' optical frame extracted from the Digitized Sky Surveys. Sources are numbered according to Table A.1. Several extended/distorted radio sources are apparent in the field. The more prominent complex is composed of the elongated structure at the North containing 13, 11, 7 and 5 which seems to join with the double structure 6/8. This complex was allready detected as a triple source by Hanisch & Ulmer (1985). At the very North, another double/tailed system is identified at the limit of the field extending North of source 3 towards source 20 at the immediate vicinity of the field. The second remarkable extended system consists of sources 15/14/12 tracing a curved structure which seems to embed source 10. At lower contrast,

Table A.1. Radiosources with a peak excess brighter than 2.5 mJy/beam detected by the NVSS in a 30' field around A 521

Number	$\alpha(J2000.0)$	$\delta(J2000.0)$	$flux$ (mJy)	a	b	**NVSS identification**
1	$04^h53^m26.80^s$	$-10°14'20.7''$	47.1	19.3	19.0	NVSSJ045326-101420
2	$04^h53^m44.51^s$	$-10°26'5.5''$	14.4	30.2	20.6	NVSSJ045344-102605
3	$04^h53^m53.28^s$	$-09°59'22.3''$	21.3	127.2	33.2	NVSSJ045353-095922
4	$04^h54^m2.46^s$	$-10°02'14.6''$	5.8	45.1	30.6	NVSSJ045402-100214
5	$04^h54^m4.80^s$	$-10°07'55.2''$	16.7	20.7	18.7	NVSSJ045404-100755
6	$04^h54^m10.78^s$	$-10°04'18.4''$	6.1	65.6	36.4	NVSSJ045410-100418
7	$04^h54^m10.84^s$	$-10°06'51.3''$	16.9	30.1	25.9	NVSSJ045410-100651
8	$04^h54^m11.74^s$	$-10°02'59.9''$	3.4	41.1	41.0	NVSSJ045411-100259
9	$04^h54^m15.45^s$	$-10°27'10.6''$	9.2	33.8	24.1	NVSSJ045415-102710
10	$04^h54^m16.21^s$	$-10°16'6.6''$	15.9	25.5	22.9	NVSSJ045416-101606
11	$04^h54^m16.28^s$	$-10°06'16.4''$	42.7	43.5	20.5	NVSSJ045416-100616
12	$04^h54^m18.77^s$	$-10°17'55.1''$	4.1	76.2	38.4	NVSSJ045418-101755
13	$04^h54^m19.87^s$	$-10°05'37.9''$	9.0	127.3	35.3	NVSSJ045419-100537
14	$04^h54^m20.23^s$	$-10°17'1.6''$	4.2	100.	64.4	NVSSJ045420-101701
15	$04^h54^m21.84^s$	$-10°15'48.0''$	7.0	72.0	53.4	NVSSJ045421-101548
16	$04^h54^m29.80^s$	$-10°13'9.6''$	3.7	53.7	39.5	NVSSJ045429-101309
17	$04^h54^m41.17^s$	$-10°01'37.3''$	10.8	34.5	23.0	NVSSJ045441-100137
18	$04^h54^m46.55^s$	$-10°20'27.8''$	3.0	83.0	45.6	NVSSJ045446-102027
19	$04^h54^m55.36^s$	$-10°13'50.7''$	1.8	36.8		NVSSJ045455-101350
20	$04^h53^m52.16^s$	$-09°57'54.8''$	23.5	47.0	24.6	NVSSJ045352-095754

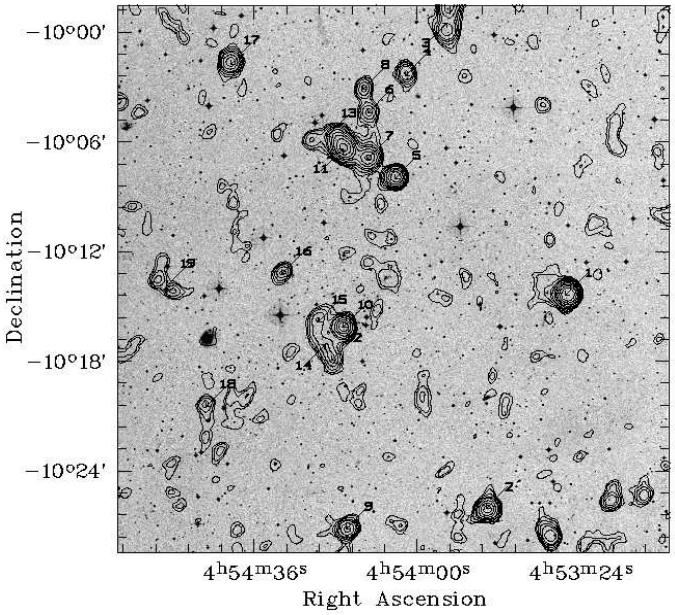

Fig. A.1. Radio contours at 1.4 GHz computed from the NVSS are superimposed to the DSS 30' field centered on the BCG of A 521. The FWHM of the Gaussian synthesized beam is $\theta = 45''$. Contour levels are: 2^0, $2^{1/2}$, 2^1, $2^{3/2}$,2^2,$2^{5/2}$,2^3,... mJy/beam. The noise r.m.s. in the radio map is 0.45 mJy/beam.

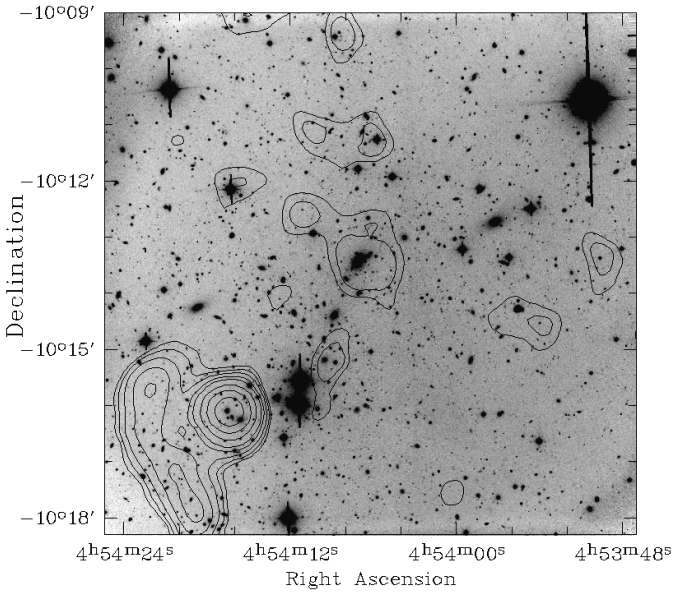

Fig. A.2. Radio contours at 1.4 GHz computed from the NVSS are superimposed to the V image obtained at CFHT. The FWHM of the Gaussian synthesized beam is $\theta = 45''$. Contour levels are: 2^0, $2^{1/2}$, 2^1, $2^{3/2}$,2^2,$2^{5/2}$,2^3,... mJy/beam. The noise r.m.s. in the radio map is 0.45 mJy/beam.

source 19 seems to consist in reality in two tailed sources. A comparison to the X-Ray map shows that no significant peak in X-Ray do correspond to any of the previous radio-sources. There is no strong radio peak centered on neither of the two X-ray maxima. Looking at the isodensities maps do not show any significant correlation between the orientation of these radio-sources and the previous detected ridges. However, most of the sources detected by NVSS are outside the CFHT central field, at about 7' of the BCG, except the 10/12/14/15 complex. Fig. A.2 shows a close-up of the radio-contours superimposed on the CFHT field previously studied. Most high density peaks in the

South-East part of the optical field are embedded within the 10/12/14/15 complex. Several clumps at North too are likely to correspond to local excesses of radio emission. The bright radio-source 10 has an optical counterpart with unfortunately no velocity measured. A 2σ enhancement in the NVSS image can be detected in the BCG. An interesting feature is that the radio isocontour shows the same North-East elongation as the HRI contour (Fig. 10). However, the radio-emission is well centered on the BCG whence the X-Ray has been shown to be offset of about 30". From this analysis, it seems that A521 presents numerous radio properties of possible interest, but radio observations of the field with a better resolution are required in order to better characterize these sources and to be able to constrain the dynamical state of the cluster.

References

Abell G.O., Corwin H.G., Olowin R.P., 1989, ApJS 70, 1
Arnaud M., Rothenflug R., Boulade O., Vigroux L., Vangioni-Flam E., 1992, A&A 254, 49
Arnouts S., de Lapparent V., Mathez G., et al., 1997, A&AS 124,163
Avni Y., 1976, ApJ 210, 642
Batuski D., Burns J., 1985, AJ 90, 1413
Batuski D., Maurogordato S., Balkowski C., Olowin R., 1995, A&A 294, 677
Batuski D., Miller C., Slinglend K., et al., 1999, submitted to ApJ
Beers T., Flynn K., Gebhardt K., 1990, AJ 100, 32
Bertin E., Arnouts S., 1996, A&AS 117, 393
Bijaoui A., Rué F., 1995, Signal Processing 46, 3, 345
Biviano A., Durret F., Gerbal D., et al., 1996, A&A 311, 95
Briel U.G., Henry J.P., 1994, Nature 372, 439
Buote D., Tsai J., 1996, ApJ 458, 27
Buote D., Xu G., 1997, MNRAS 284, 439
Burns J., Rhee G., Owen F., Pinkney J., 1994, ApJ 423, 94
Burns J.O., Roettiger K., Pinkney J., et al., 1995, ApJ 446, 58
Condon J.J., Cotton W.D., Greisen E.W., et al., 1996, ADIL, JC, 01
Condon J.J., Cotton W.D., Greisen E.W., et al., 1998, AJ 115, 1693
Dantas C., de Carvalho E., Capelato H., Mazure A., 1997, ApJ 485, 447
David L.P., Harnden F.R., Kearns K.E., Zombeck M.V., 1993, The ROSAT High Resolution Imager (HRI), (USRSDC, SAO)
Dickey J.M., Lockman F.J., 1990, ARA&A 28, 215
Dressler A., 1980, ApJ 236, 351
Durret F., Forman W., Gerbal D., Jones C., Vikhlinin A., 1998, A&A 335, 41
Escalera E., Slezak E., Mazure A., 1992, A&A 264, 379
Feretti L., Boehringer H., Giovannini G., Neumann D., 1997, A&A 317, 432
Feretti L., Giovannini G., 1996, In: Ekers R., Fanti C., Padrielli L. (eds.) Extragalactic Radio Sources. IAU Symp. 175, Kluwer Academic Publisher
Friel E., Heasley J.N., Christian C.A., 1987, PASP 99, 1248
Galaz G., 1997, Ph.D. Thesis, Paris VI University
Gambera M., Pagliaro A., Antonuccio-Delogu V., Becciani U., 1997, ApJ 488, 136
Hanisch R.J., Ulmer M.P., 1985, ApJ 90, 1407
Jones C., Forman W., 1984, ApJ 276, 38
Jones C., Forman W., 1999, ApJ 511, 65
Katz N., White S.D.M., 1993, ApJ 412, 455
Kowalski M.P., Ulmer M.P., Cruddace R.G., Wood K.S., 1984, ApJS 56, 403
Le Fèvre O., Bijaoui A., Mathez G., Picat J.P., Lelievre G., 1986, A&A 154, 92
Lemonon L., Pierre M., Hunstead R., et al., 1997, A&A 326, 34
Lima Neto G., Pislar V., Durret F., Gerbal D., Slezak E., 1997, A&A 327, 81
Lubin L., Bahcall N., 1993, ApJ 415, L17
Maurogordato S., Le Fevre O., Proust D., Vanderriest C., Cappi A., 1996, BCFHT 34, 6
Maurogordato S., Proust D., Beers T.C., et al., 1998, A&A submitted, astro-ph/9901378
Mohr J.J., Evrard A.E., Fabricant D.G., Geller M.J., 1995, ApJ 447, 8
Nakamura F.E., Hattori M., Mineshige S., 1995, A&A 302, 649
Pierre M., Starck J.L., 1998, A&A 330, 801
Pinkney J., Rhee G., Burns J.O., et al., 1993, ApJ 416, 36
Pislar V., Durret F., Gerbal D., Lima-Neto G., Slezak E., 1997, A&A 322, 53
Plionis M., et al., 1999 in preparation
Quintana H., Ramirez A., 1995, ApJS 96, 343
Richstone D., Loeb A., Turner E.L., 1992, ApJ 393, 477
Roettiger K., Loken C., Burns J., 1997, ApJS 109, 307
Rué F., Bijaoui A., 1997, Experimental Astronomy 7, 129
Sandage A., Perelmuter J.M., 1990, ApJ 350, 481
Schindler S., Böhringer H., 1993, A&A 269, 83
Schindler S., Muller E., 1993, A&A 272, 137
Slezak E., Bijaoui A., Mars G., 1990, A&A 227, 301
Slezak E., Durret F., Gerbal D., 1994, AJ 108, 1996
Slezak E., Durret F., Guibert J., Lobo C., 1998, A&AS 128, 67
Snowden S.L., 1995, Cookbook for analysis procedures for ROSAT XRT/PSPC observations of extended objects and the diffuse background. NASA/GSFC, USRSDC
Snowden S.L., 1998, ApJS 117, 233
Strubble M., Rood H., 1982, AJ 87, 7
Strubble M., Rood H., 1987, ApJS 63, 543
Strubble M., Rood H., 1991, ApJS 77, 363
Ulmer M.P., Kowalski M.P., Cruddace R.G., 1986, ApJ 303, 162
Ulmer M.P., Cruddace R.G., Kowalski M.P., 1985, ApJ 290, 551
van Haarlem M., van de Weygaert R., 1993, ApJ 418, 544
Vrtilek J.M., David L., Vikhlinin A., Forman W., Jones C., 1997, A&AS 191, 5304
Vikhlinin A., Forman W., Jones C., 1997, ApJ 474, L7
West M.J., Villumsen J.V., Dekel A., 1991, ApJ 369, 287
West M.J., Jones C., Forman W., 1995, ApJ 451, L5